Extraction of singular points from dense motion fields: an analytic approach

T. Corpetti (tcorpett@irisa.fr)
IRISA/Université de Rennes I, Campus universitaire de Beaulieu,35042 Rennes Cedex, France

E. Mémin (memin@irisa.fr)
IRISA/Université de Rennes I, Campus universitaire de Beaulieu,35042 Rennes Cedex, France

P. Pérez (pperez@microsoft.com)
Microsoft Research, St George House, 1 Guildhall Street, Cambridge, CB2 3NH, UK

Abstract. *In this paper we propose a new method to extract the vortices, sources, and sinks from the dense motion field preliminary estimated between two images of a fluid video. This problem is essential in meteorology for instance to identify and track depressions or convective clouds in satellite images. The knowledge of such points allows in addition a compact representation of the flow which is very useful in both experimental and theoretical fluid mechanics. The method we propose here is based on an analytic representation of the flow. This approach has the advantage of being robust, simple, fast and requires few parameters.*

Keywords: Fluid motion, singular points, stream function, velocity potential, Rankine model.

1. Introduction

Since several years, the analysis of video sequences showing the evolution of fluid phenomenon gave rise to a great attention from the image analysis community [9, 12, 16, 18, 31]. The applications concern domains such as experimental visualization in fluid mechanics, environmental sciences (oceanography, meteorology,...), or medical images. In all these application domains, it is of primary interest to measure the instantaneous velocity of fluid particles. In oceanography one is interested to track sea streams and to observe the drift of some passive entities [11, 28]. In meteorology, both operational and experimental the task under consideration is the reconstruction of wind fields from the displacements of clouds as observed in various satellite images [3, 23, 27]. In medical imaging the issue is to visualize and analyze blood flow inside the heart, or inside blood vessels [13, 29]. The images involved in each domain have their own characteristics and are provided by very different sensors. The huge amount of data of different kinds available, the range of applicative domains involved, and the technical difficulties in the processing of all these peculiar image sequences explain the interest of researchers of the image analysis community.

In this context, one problem of interest is the extraction and the characterization of the *critical* – or *singular* – points of the flow. These points are the centers of kinematical events such as *swirl*, *vortices* or *sinks/sources*. The latter correspond to areas of apparent diverging 2D motions which are either related to 3D motions not parallel to the image plane or to real sinks or sources of matter. The knowledge of the type and location of these points is for instance of great interest in meteorology to detect and track violent and sudden meteorological events such as convective clouds or tornados[19, 24]. The knowledge of all these points is thus precious to understand and predict the flows of interest. It also allows for compact and hierarchical representations of the flow [16, 15, 14, 22].

Most of the methods used so far to localize and characterize critical points are based on local linear *phase portrait* approximation of the flow around points where the velocity vanishes (singular points). These techniques have been pioneered by Rao and Jain's work [25] originally proposed in the context of wood or wafer inspection. The authors developed a non linear least squares technique to estimate a first-order flow model from the oriented texture field. It is associated to a vote technique to locate and classify critical points. The approach has been extended to fluid images by Ford *et.al* for linear [16] and non-linear phase portraits [15]. The localization of critical points is here based on the use of Poincaré index (or winding number). Winding number technique has also been used from previously estimated dense velocity fields together with a phase portrait model [9] or without it [21]. Maurizot *et. al.* [19] proposed a statistical method based on the study of bias and variance of a risk function. This method allows to compute simultaneously a linear phase portrait, the critical point location, and a rectangular domain of linearity around each point. This method is less sensitive to noise due to its statistical nature. Nevertheless unlike index technique it does not allow formally to recover all the singular points of the flow. In practice only the most "attractive" ones are captured. Another method based on analytic modeling of the flow and the *Cauchy*'s theorem of residues has been proposed in [22] in the context of medical images. Based on our experience, this approach is unfortunately very sensitive to noise.

As in this latter work, the technique we propose to detect and characterize vortices, sinks and sources relies on a complex modeling of the velocity field. Not only it allows a robust extraction and identification of singular points, but it also enables to build a compact parametric representation of the velocity field. This parametric representation is based on the *Rankine* model of vortex.

The paper is organized as follows. After recalling some basic definitions and properties of planar vector fields on which our work relies, we show how the velocity fields may be separated into its two *solenoidal* and *irrotational* components which gather respectively the divergence and the vorticity of the velocity field. We show also how the location of the critical points may be obtained as local extrema of a *complex potential* function of the flow. It is shown also how this methodology allows to get access to additional information on the flow such as *streamlines*. A second part is devoted to the presentation of the *Rankine* model and to its estimation from a dense velocity field. In the last part of the paper, the performance of the method is demonstrated on different kinds of meteorological image sequences.

2. Planar vector fields

The method we propose in this paper aims at the recovery of vortices and sinks/sources of a previously estimated instantaneous velocity fields. We will consider only 2D fields defined over the bounded image plane.

A lot of techniques exist in the literature to estimate a 2D dense motion field from a sequence of images. In the field of experimental visualization in fluid mechanics, most of the methods are correlation based [1]. The displacement of a fluid element is obtained by maximizing a local correlation function. In meteorology, such methods are also used to recover wind fields from cloud tracking [23, 26]. These methods are fast, but lead usually to sparse and sometimes inaccurate motion fields due to the necessary quantization of velocities. The sparse and quantized nature of the motion field prevents from recovering accurately valuable information such as trajectories, streamlines, vorticity, or divergence of the flow.

Dense motion field estimators for fluid flows have also been studied by the computer-vision community. These estimators are essentially based on the seminal work of Horn and Schunck [17]. They resort to the minimization of an objective functional composed of two terms. A data term based on a photometric consistency assumption and a regularization term which enforces the smoothness of the solution. Recently functionals dedicated to fluid images have been proposed [6, 10]. They incorporate a dedicated data-term based on the continuity equation of fluid mechanics. Additional improvements are obtained by considering tailor-made regularization terms preserving the concentrations of divergence and vorticity [10].

Before explaining the core of our method to recover and characterize the singularities of the flow, let us review some useful definitions and properties of planar vector fields.

2.1. Definitions and properties

A planar vector field $\boldsymbol{\omega}$ is a $I\!R^2$-valued map defined on a bounded set Ω of $I\!R^2$ and we should denote $\boldsymbol{\omega}(x,y) \triangleq (u(x,y), v(x,y))$ where x and y stands for the spatial coordinates. The flow of a fluid is the vector field of instantaneous velocities. If the flow is unsteady then the velocity depends on time as well on position, and we should note $\boldsymbol{\omega}(x,y,t)$. In the following, unless specified otherwise, we always refer to time dependent vector fields. For the sake of simplicity we will therefore omit the time index. Throughout the paper we will also suppose that each component of the vector field is twice continuous and differentiable: u and $v \in C^2(\Omega, I\!R)$.

The operator $\boldsymbol{\nabla}$ denotes the symbolic vector operator whose components are the partial derivatives with respect to x and y coordinates: $\boldsymbol{\nabla} = (\frac{\partial}{\partial x}, \frac{\partial}{\partial y})$. If $\boldsymbol{\nabla}$ operates on a scalar field $\phi(x,y)$ one gets a vector field $\boldsymbol{\nabla}\phi(x,y) = (\frac{\partial \phi(x,y)}{\partial x}, \frac{\partial \phi(x,y)}{\partial y})$ which is the gradient of a scalar field. The symbolic dot product $\mathrm{div}(\boldsymbol{\omega}) \triangleq \boldsymbol{\nabla} \cdot \boldsymbol{\omega} = \frac{\partial u}{\partial x} + \frac{\partial v}{\partial y}$ is the *divergence* of the vector field. The integral of this quantity over a region $\mathcal{R}$ amounts to compute the flux of the vector field across the boundary of the region $\partial\mathcal{R}$ (*divergence theorem*):

$$\iint_{\mathcal{R}} \mathrm{div}(\boldsymbol{\omega}) = \int_{\partial\mathcal{R}} \boldsymbol{\omega} \cdot \boldsymbol{n}, \tag{1}$$

where $\boldsymbol{n}$ denotes the outward normal to the boundary $\partial\mathcal{R}$. A vector field whose divergence is null everywhere is called *solenoidal*.

In a similar way, noting $\boldsymbol{\omega}^{\perp} \triangleq (-v, u)$ the orthogonal counterpart of $\boldsymbol{\omega}$, we define the *vorticity* of the vector field as the quantity: $\mathrm{curl}(\boldsymbol{\omega}) \triangleq \boldsymbol{\nabla} \cdot \boldsymbol{\omega}^{\perp} = \frac{\partial u}{\partial y} - \frac{\partial v}{\partial x}$. Its integral over a simply connected region $\mathcal{R}$ is equivalent to the circulation of the vector along the region boundary (*Green theorem*):

$$\iint_{\mathcal{R}} \mathrm{curl}(\boldsymbol{\omega}) = \int_{\partial\mathcal{R}} \boldsymbol{\omega} \cdot \boldsymbol{\tau}, \tag{2}$$

where $\boldsymbol{\tau}$ denotes the unitary tangent along the closed curve $\partial\mathcal{R}$. A vector field whose curl vanishes identically is called *irrotational*.

For irrotational vector fields, the application of Green theorem shows that the circulation of the vector along a closed curve is null. The circulation along an arc joining two points depends therefore only on these two end points. In particular, one can define uniquely a function $\phi(x, y)$ giving the circulation of $\boldsymbol{\omega}$ along an arbitrary path from the origin to (x, y). The circulation on a path with endpoints p and q is then $\phi(p) - \phi(q)$. Considering the circulation of $\boldsymbol{\omega}$ along an infinitesimal arc parallel to x, we have:

$$\frac{\partial \phi}{\partial x} = \lim_{\Delta x \to 0} \frac{1}{\Delta x}[\phi(x + \Delta x, y) - \phi(x, y)] = \lim_{\Delta x \to 0} \frac{1}{\Delta x} \int_{x}^{x+\Delta x} u(t, y) dt = u(x, y).$$

Using the same technique along y one thus gets the classical result that for irrotational fields there exists a scalar function ϕ, called the *velocity potential*, such that:

$$\boldsymbol{\omega} = \boldsymbol{\nabla} \phi. \tag{3}$$

The velocity at point $\boldsymbol{s} = (x, y)$ is therefore orthogonal to the curve $\{\phi(x, y) = c\}$. These curves are normal to the integral lines of the velocity field (*i.e.* the streamlines, or the trajectories for steady flows).

Now, if $\boldsymbol{\omega}$ is solenoidal it is easy to see that the field $\boldsymbol{\omega}^{\perp}$ is irrotational and therefore, there exists a scalar function ψ, called the *stream function* such that:

$$\boldsymbol{\omega}^{\perp} = \boldsymbol{\nabla} \psi. \tag{4}$$

The equipotential curves, $\{\psi(x, y) = c\}$, are the streamlines of the flow. For a flow both irrotational and solenoidal, it is interesting to note that level curves of ϕ and ψ form an orthogonal network.

2.2. Complex potential

If the field is both irrotational and solenoidal from equations (3) and (4) we deduce:

$$\frac{\partial \phi}{\partial x} = \frac{\partial \psi}{\partial y} \quad \text{and} \quad \frac{\partial \phi}{\partial y} = -\frac{\partial \psi}{\partial x}. \tag{5}$$

These equations are the *Cauchy* conditions that must be satisfied for the function:

$$F(z) \triangleq \phi(x, y) + i\psi(x, y), \tag{6}$$

of the complex variable $z = x + iy$ to be *z-differentiable* or *analytic*. Its complex derivative is:

$$F'(z) = \frac{\phi(x, y)}{\partial x} + i\frac{\psi(x, y)}{\partial y} = \overline{f(z)} = u(x, y) - iv(x, y),$$

that is the complex conjugate of the complex representation of the velocity field $f(z) = u(x, y) + iv(x, y)$. The knowledge of this function $F(z)$, called the *complex potential*, provides a triple advantage. By derivation it gives the velocity, and it allows to obtain without any computation the curves $\{\phi(x, y) = c\}$ and their orthogonal counterpart, the streamlines $\{\psi(x, y) = c\}$. It might be therefore very fruitful and practical to describe the velocity field as complex functions. We will rely on a peculiar case of such a modeling in the following section.

Irrotational and solenoidal fields play an important role in vector field analysis. As a matter of fact these two types of fields can be combined to represent uniquely any arbitrary continuous vector field which vanishes at infinity. This is the *Helmholtz* representation of vector fields $\boldsymbol{\omega} = \boldsymbol{\omega}_{so} + \boldsymbol{\omega}_{ir}$. For any vector field $\boldsymbol{\omega}$ one can define the velocity potential ϕ of its irrotational component, and the stream function ψ of its solenoidal component. As a result, the complex potential $F = \phi + i\psi$ can be defined. It reduces to a real function for irrotational flow and to a pure imaginary function for solenoidal vector fields. The complex function is nevertheless not anymore analytic and the velocities are then obtained from equation (3) and (4) *i.e*, $\boldsymbol{\omega}_{ir} = \boldsymbol{\nabla}\phi$, $\boldsymbol{\omega}_{so} = \boldsymbol{\nabla}\psi$.

When the null border condition at infinity cannot be imposed, the representation is extended by the introduction of a third *laminar* component. A laminar field is a vector field that is both irrotational and solenoidal. The extended *Helmholtz* representation is then:

$$\boldsymbol{\omega} = \boldsymbol{\omega}_{lam} + \boldsymbol{\omega}_{so} + \boldsymbol{\omega}_{ir}. \tag{7}$$

In our applications, the laminar component accounts for a global transportation flow and for the effect of sources/sinks or vortices outside of the image plane. In the following we assume that this very smooth component is known. It is indeed easy to estimate a laminar component from a pair of images, and many techniques from computer vision are available. For example, one can use a standard motion estimation technique based on Horn and Schunck model (as the one in [20]) under a strong first order regularization and whose rule is to prevent from the apparition of diverging and rotationnal motion fields. In this work, we used a particular case of a technique proposed in [10], which, through an adequate regularization prior, strongly enforces a null divergence together with a null curl. The resulting motion field can be associated to the laminar part of the flow. From now we will always refer to motion fields vanishing at infinity, and consequently to the original Helmholtz representation.

2.3. Irrotational and solenoidal field separation

Equation (3) and (4) characterize respectively irrotational fields and solenoidal fields. The potential functions ϕ and ψ of a given continuous vector field $\boldsymbol{\omega}$ are therefore related to its irrotational and solenoidal part respectively. Taking the divergence of (3) and (4) leads to

$$\boldsymbol{\nabla}^2\phi = \mathrm{div}(\boldsymbol{\omega}) \quad \text{and} \quad \boldsymbol{\nabla}^2\psi = \mathrm{curl}(\boldsymbol{\omega}). \tag{8}$$

Both potential functions are therefore the solution of Poisson equations. Assuming that the curl and divergence vanish at infinity, one has to face a well known Dirichlet problem whose solution may be obtained through 2D Green kernel:

$$h(x,y) = \frac{1}{2}\ln(x^2+y^2). \tag{9}$$

With that kernel and noting $\boldsymbol{\nabla}^\perp = (-\frac{\partial}{\partial y}, \frac{\partial}{\partial x})$, one can define two orthogonal vector fields:

$$\begin{aligned}
\boldsymbol{w}_1(x,y) &= \frac{1}{2\pi}\int_{-\infty}^{\infty}\int_{-\infty}^{\infty} \boldsymbol{\nabla}h(x-u,y-v)\mathrm{div}\boldsymbol{\omega}(x,y)dudv \\
\boldsymbol{w}_2(x,y) &= \frac{1}{2\pi}\int_{-\infty}^{\infty}\int_{-\infty}^{\infty} \boldsymbol{\nabla}^\perp h(x-u,y-v)\mathrm{curl}\boldsymbol{\omega}(x,y)dudv,
\end{aligned} \tag{10}$$

which have the same divergence and curl as $\boldsymbol{\omega}$ and which vanish at infinity. Assuming the vector field $\boldsymbol{\omega}$ has bounded components, it is easy to prove that it is uniquely specified by its divergence and curl and consequently $\boldsymbol{w}_1 = \boldsymbol{w}_{ir}$ and $\boldsymbol{w}_2 = \boldsymbol{w}_{so}$.

To show this, let us denote any vector fields $\boldsymbol{f}_1$ and $\boldsymbol{f}_2$ with exactly the same curl and divergence and which both tend to zero at infinity; let also the field $\boldsymbol{d} = \boldsymbol{f}_1 - \boldsymbol{f}_2$ be their difference. Assuming that $\boldsymbol{d}$ is continuously differentiable, then it admits an analytic complex potential (as div $\boldsymbol{d} = 0$ and curl $\boldsymbol{d} = 0$) $F(z) = P(x,y) + iQ(x,y)$. From Liouville theorem we know that any bounded analytic function over the whole complex plane is constant. Therefore, $F(z)$ is constant and $\boldsymbol{d} = \overline{F'}$ is null everywhere.

Knowing the divergence and the curl of a velocity field, the extraction of the irrotational and the solenoidal components through convolutions (10) may be numerically tricky since it lies on infinite support.

Instead of that, using a spectral *Fourier* representation of the flow $\hat{\boldsymbol{\omega}} = (\mathcal{F}[u], \mathcal{F}[v])$ such that:

$$\hat{f}(\boldsymbol{k}) = \mathcal{F}[f] = \frac{1}{2\pi} \iint f(\boldsymbol{s}) e^{j<\boldsymbol{k},\boldsymbol{s}>} d\boldsymbol{s}, \text{and} f(\boldsymbol{s}) = \frac{1}{2\pi} \iint \hat{f}(\boldsymbol{k}) e^{-j<\boldsymbol{k},\boldsymbol{s}>} d\boldsymbol{k} \tag{11}$$

with $\boldsymbol{k} = (\alpha, \beta)$, (α, β) being the frequencies coordinates of (x, y). In the Fourier domain, we have:

$$\begin{aligned} \mathcal{F}[\text{curl}(\boldsymbol{\omega})] = \mathcal{F}[\text{curl}(\boldsymbol{\omega}_{ir})] &= <\boldsymbol{k}^{\perp}, \hat{\boldsymbol{\omega}}_{ir}(\boldsymbol{k})> = 0, \\ \mathcal{F}[\text{div}(\boldsymbol{\omega})] = \mathcal{F}[\text{div}(\boldsymbol{\omega}_{so})] &= <\boldsymbol{k}, \hat{\boldsymbol{\omega}}_{so}(\boldsymbol{k})> = 0. \end{aligned} \tag{12}$$

Therefore, assuming the vector field $\boldsymbol{\omega}$ is known, the irrotational and the solenoidal component may be respectively obtained through:

$$\hat{\boldsymbol{\omega}}_{ir}(\boldsymbol{k}) = <\boldsymbol{k}, \hat{\boldsymbol{\omega}}(\boldsymbol{k})> \frac{\boldsymbol{k}}{\|\boldsymbol{k}\|^2} \tag{13}$$

and

$$\hat{\boldsymbol{\omega}}_{so}(\boldsymbol{k}) = <\boldsymbol{k}^{\perp}, \hat{\boldsymbol{\omega}}(\boldsymbol{k})> \frac{\boldsymbol{k}^{\perp}}{\|\boldsymbol{k}^{\perp}\|^2}. \tag{14}$$

The irrotational and solenoidal components are finally obtained from the inverse Fourier transform.

It is important to note that Fourier transform is defined for periodic signals. When the motion field is non-periodic (which is the case in practice), classical techniques consists to add identically end to end the motion field in order to apply the Fourier transform on the resulting periodic signal. To attenuate boundary effects that may appear as a consequence of this manipulation, it is usual to apply this kind of technique on a larger motion field that contain the original one, bordered with zeros on the whole sides long. This way, connections between two consecutive fields are softer and attenuate the apparition of non-desired signals in the Fourier domain. In practice, for an original motion field whose size is $(N \text{ x } M)$, we use a is $(4N \text{ x } 4M)$ for the Fourier transform.

2.4. Potential functions estimation

As it has been shown in the previous section, the knowledge of the complex potential function and more generally of its components ϕ and ψ might be very useful as it allows a complete description of the velocity field. In turn, if the velocity field and its irrotational and solenoidal components are known, functions ϕ and ψ can be easily estimated(as $\boldsymbol{w}_{ir} = \boldsymbol{\nabla}\phi$ and $\boldsymbol{w}_{so}^{\perp} = \boldsymbol{\nabla}\psi$). Noting that, if g is a C^2 function, $g(x, y) =$

$g(0,0) + \int_\gamma \nabla g(x,y) \cdot d\gamma$, where γ is any path from $(0,0)$ to (x,y). Averaging this relation over the two paths joining $(0,0)$ to (x,y) along the sides of a rectangle, we get:

$$\begin{cases} \phi(x,y) = \frac{1}{2}\Big(\int\limits_0^x u_{ir}(t,y)dt + \int\limits_0^y v_{ir}(x,t)dt \\ \qquad + \int\limits_0^x u_{ir}(t,0)dt + \int\limits_0^y v_{ir}(0,t)dt \Big) + \phi(0,0), \text{ and} \\ \psi(x,y) = \frac{1}{2}\Big(\int\limits_0^y u_{so}(x,t)dt - \int\limits_0^x v_{so}(t,y)dt \\ \qquad + \int\limits_0^y u_{so}(0,t)dt - \int\limits_0^x v_{so}(t,0)dt \Big) + \psi(0,0). \end{cases} \tag{15}$$

Both terms of relation (15) may be conveniently numerically computed, as they consist in 1D integrations along image rows and the columns.

2.5. Extrema of the potential function

From (3), it can be observed that characteristic points of the irrotational flow component (*i.e.*, points $\boldsymbol{s}$ for which $\boldsymbol{\omega}_{ir}(\boldsymbol{s}) = \nabla\phi(\boldsymbol{s}) = 0$) corresponds to local extremum of the velocity potential ϕ. Of course the same relationship links extremum of the stream function and characteristic points of the solenoidal component. Otherwise, around a singular point $\boldsymbol{s} = (x,y)$, the velocity distribution of a fluid flow can be accurately approximated (and characterized) by the so-called *linear phase portrait* [2]. Within some neighborhood around $\boldsymbol{s}$, one can fit a parametric velocity model of the form $\boldsymbol{\omega} = A\boldsymbol{s}$ where A is a 2×2 matrix. The qualitative characterization of the motion field in the neighborhood of this singular point $\boldsymbol{s}$ relies on the structure of matrix A. Six typical motion configurations can be identified from its canonical Jordan form [2, 16] (see figure 1)

A second-order approximation of the velocity potential and the stream function around a singular points gives respectively:

$$\boldsymbol{\omega}_{ir} = \nabla\phi(\boldsymbol{s}+\boldsymbol{\epsilon}) = H_\phi(\boldsymbol{s})\boldsymbol{\epsilon} + o(\boldsymbol{\epsilon}) \tag{16}$$

and

$$\boldsymbol{\omega}_{so}^{\perp} = \nabla\psi(\boldsymbol{s}+\boldsymbol{\epsilon}) = H_\psi(\boldsymbol{s})\boldsymbol{\epsilon} + o(\boldsymbol{\epsilon}), \tag{17}$$

eigenvalues	Jordan form	type	phase portrait
real and distinct ($\Delta(A) > 0$)	$\begin{bmatrix} \lambda_1 & 0 \\ 0 & \lambda_2 \end{bmatrix}$ $\lambda_1\lambda_2 > 0$	node $\det(A) > 0$	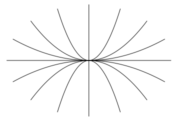
	$\begin{bmatrix} \lambda_1 & 0 \\ 0 & \lambda_2 \end{bmatrix}$ $\lambda_1\lambda_2 < 0$	saddle $\det(A) < 0$	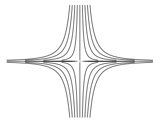
equal ($\Delta(A) = 0$)	$\begin{bmatrix} \lambda_1 & 0 \\ 0 & \lambda_1 \end{bmatrix}$	star node $\mathrm{rot}(A) = 0$	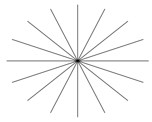
	$\begin{bmatrix} \lambda_1 & 1 \\ 0 & \lambda_1 \end{bmatrix}$	improper node $\mathrm{rot}(A) \neq 0$	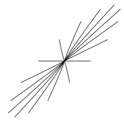
complex $\alpha \pm i\beta$ ($\Delta(A) < 0$)	$\begin{bmatrix} 0 & -\beta \\ \beta & 0 \end{bmatrix}$	center $\mathrm{tr}(A) = 0$	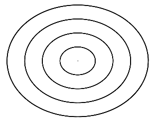
	$\begin{bmatrix} \alpha & -\beta \\ \beta & \alpha \end{bmatrix}$	spiral $\mathrm{tr}(A) \neq 0$	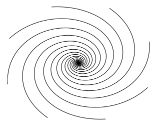

Figure 1. Singular points classification based on the structure of the linear phase portrait matrix A; $\Delta(A) \triangleq \mathrm{tr}^2(A) - 4\det(A)$.

with Hessian $H_\phi(\boldsymbol{s}) = \begin{bmatrix} \frac{\partial^2\phi}{\partial x^2} & \frac{\partial^2\phi}{\partial xy} \\ \frac{\partial^2\phi}{\partial xy} & \frac{\partial^2\phi}{\partial y^2} \end{bmatrix}$ and $H_\psi(\boldsymbol{s}) = \begin{bmatrix} \frac{\partial^2\psi}{\partial x^2} & \frac{\partial^2\psi}{\partial xy} \\ \frac{\partial^2\psi}{\partial xy} & \frac{\partial^2\psi}{\partial y^2} \end{bmatrix}$. The phase portrait of irrotational field around singular point $\boldsymbol{s}$ is given by $H_\phi(\boldsymbol{s})$. As this matrix is symmetric (since curl $\boldsymbol{\omega}_{ir} = 0$), it has real eigenvalues. Around local extrema the matrix is in addition positive or negative definite. In that case, the eigenvalues are therefore all positive or all negative. The singular point corresponding to a maxima or a minima is thus a *node* or a *star node*. For the solenoidal field the phase portrait is given by $A_\psi = \begin{bmatrix} \frac{\partial^2\psi}{\partial xy} & \frac{\partial^2\psi}{\partial y^2} \\ -\frac{\partial^2\psi}{\partial x^2} & -\frac{\partial^2\psi}{\partial xy} \end{bmatrix}$ whose trace is null: the singular point is a *center*. These three configurations characterize well the flow in the vicinity of vortices and sink/sources. The knowledge of the two potential functions gives us therefore a practical way to extract vortices, sinks or sources. As a matter of fact, to estimate those peculiar singular points one has just to identify the points corresponding to extremal values of the potential function. Unlike to Poincaré indices techniques, the other configurations – which are less informative from a physical point of view – are discarded by the proposed method since they do not correspond to extremal value of the potential functions.

3. Rankine model of flows

One of the simplest models of velocity field for fluid flows comes from the *Rankine* model of vortex. It consists in approximating the velocity field of a vortex as a vector field of constant curl inside a disk representing the shape and the location of the vortex. Beyond this circular domain the velocity decreases as the inverse squared distance to the disk center and the vorticity is null. A complex representation of this velocity field reads:

$$f_\imath(z) \triangleq \begin{cases} g_\imath(z) = -\dfrac{i\beta_\imath(z-z_\imath)}{|z-z_\imath|^2} & \text{if} \quad |z-z_\imath| \geq r_\imath \\ h_\imath(z) = -\dfrac{i\beta_\imath(z-z_\imath)}{r_\imath^2} & \text{if} \quad |z-z_\imath| < r_\imath, \end{cases} \tag{18}$$

where $r_\imath$ is the singularity radius; $z_\imath \triangleq x_\imath + iy_\imath$ denotes the complex vortex location and $\beta_\imath$ its strength. Based on a similar model the velocity field associated to, source/sink in the plane can modeled as:

$$f_\jmath(z) \triangleq \begin{cases} g_\jmath(z) = \dfrac{\alpha_\jmath(z-z_\jmath)}{|z-z_\jmath|^2} & \text{if} \quad |z-z_\jmath| \geq r_\jmath \\ h_\jmath(z) = \dfrac{\alpha_\jmath(z-z_\jmath)}{r_\jmath^2} & \text{if} \quad |z-z_\jmath| < r_\jmath \end{cases} \tag{19}$$

where $\alpha_\jmath$ denotes the sink/source's strength. If $\alpha_\jmath > 0$, this constitutes a source model, whereas if $\alpha_\jmath < 0$ we are in presence of a sink. From these equations it is easy to verify that functions $f_\imath$ are solenoidal (*i.e.*,

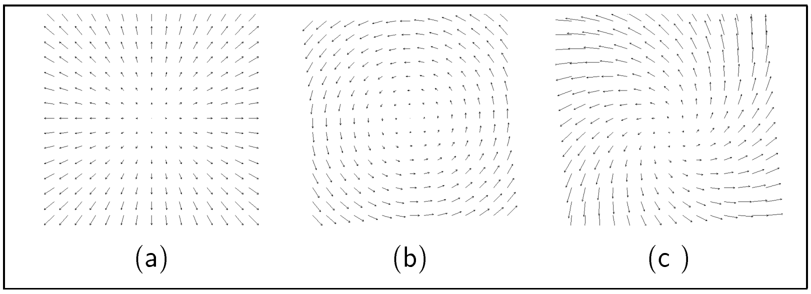

Figure 2. Velocity fields associated to (a) a source, (b) a vortex , and to (c) the composition of a source and of a vortex .

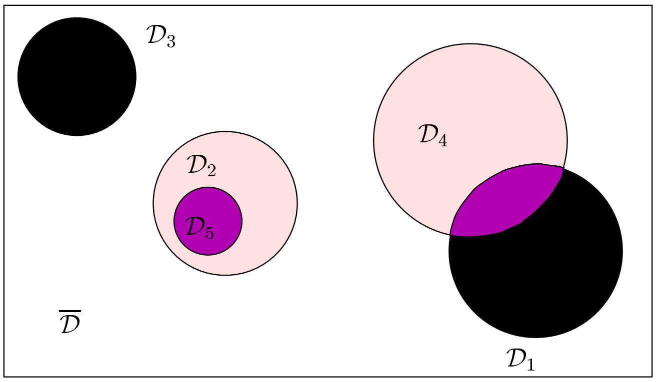

Figure 3. Example of *Rankine* models supports; disks associated to vortices are light-colored whereas sources/sinks are in black; intermediary-colored regions denote areas where the curl and the divergence are simultaneously non-null.

$\text{div}(f_i) = 0$) whereas functions f_j are irrotational (*i.e.*, $\text{curl}(f_j) = 0$). The functions h_i (respectively h_j) are of constant curl, $\text{curl}(\boldsymbol{\omega}) = \frac{2\beta_i}{r_i^2}$, (resp. of constant divergence, $\text{div}(\boldsymbol{\omega}) = \frac{2\alpha_j}{r_j^2}$) whereas functions g_i (resp. g_j) have a null divergence and vorticity everywhere.

These two fields can be composed to model a fluid flow with P vortices and N sources/sinks:

$$f(z) = \sum_{i=1}^{P} f_i(z) + \sum_{j=1}^{N} f_j(z). \tag{20}$$

The figure 2 shows examples of fields associated respectively with a vortex, a source and, a composition of both entities at the same location.

3.1. Velocity potential and stream-function

From the *Rankine* model expression, it is informative to deduce the associated potential functions. To that end, it is necessary to consider separately the possible different cases.

3.1.0.1. *Vortex model*

Let us consider a Rankine vortex centered at $z_\imath = 0$ (for simplicity) and of radius $r_\imath$ and strength $\beta_\imath$. According to equation (18), the associated velocity field outside of the disk reads:

$$\begin{aligned} f(x+iy) &= \beta_\imath\Big(\frac{y}{x^2+y^2} - i\frac{x}{x^2+y^2}\Big) \\ &= u(x,y) + iv(x,y) \end{aligned} \tag{21}$$

According to equation (15) and recalling that:

$$\begin{cases} \displaystyle\int \frac{y}{x^2+y^2}dx = \mathrm{Arctan}(\frac{x}{y}) \\ \displaystyle\int \frac{y}{x^2+y^2}dy = \frac{1}{2}\ln(x^2+y^2), \end{cases} \tag{22}$$

one gets:

$$\begin{cases} \phi(x,y) = \beta_\imath \mathrm{Arctan}(\dfrac{x}{y}) \\ \psi(x,y) = \dfrac{\beta_\imath}{2}\ln(x^2+y^2), \end{cases} \tag{23}$$

which gives us the associated complex potential

$$F(z) = \phi(x,y) + i\psi(x,y) = i\beta\ln(z). \tag{24}$$

Inside a vortex disk we have now $f(x+iy) = -\frac{i\beta}{r^2}(x+iy)$. Integrating in the same way function $u(x,y)$ and $v(x,y)$ we obtain:

$$\begin{cases} \phi(x,y) = 0 \\ \psi(x,y) = \dfrac{\beta}{2r^2}(x^2+y^2) \end{cases} \tag{25}$$

3.1.0.2. *Source/sink model*

In a similar way, we obtain the complex potential component associated to a sink/source. Outside of the circular linearity domain centered at the origin and representative of a source/sink of strength $\alpha_\jmath$ we have the velocity potential and the stream function given by:

$$\begin{cases} \phi(x,y) = \dfrac{\alpha}{2}\ln(x^2+y^2) \\ \psi(x,y) = \alpha \mathrm{Arctan}(\dfrac{y}{x}) \end{cases} \tag{26}$$

The complex potential is therefore $F(z) = \phi(x,y) + i\psi(x,y) = \alpha \ln(z)$.

Inside of this circular domain the velocity potential and the stream function are:

$$\begin{cases} \phi(x,y) = \dfrac{\alpha}{2r^2}(x^2+y^2) \\ \psi(x,y) = 0 \end{cases} \tag{27}$$

From these expressions it may be check that outside the different circles the functions ϕ and ψ do not have any local minima/maxima whereas inside the disks each function respectively admits local maxima/minima at the disk centers. These centers correspond to the location of singular points associated to vortices, sinks or sources of the flow.

3.2. Rankine model estimation from a velocity field

As recalled in section §2 the knowledge of the instantaneous velocity field $\boldsymbol{\omega}$ of a fluid flow enables to recover its associated stream-function and velocity potential. We saw also that the knowledge of both potential functions gives a practical way to identify all the vortices and sinks/sources of the flow by extracting their minima and maxima. In addition, in order to define completely the flow in terms of its Rankine parametric representation we need now to estimate the strength and the circular linearity domain associated to the different singular points.

To that end, we will first assume that the field $\boldsymbol{\omega}$ previously estimated from a dense estimator such as [10] has been separated into its two irrotationnal and solenoidal components by means of equations (13) and (14). Considering now these two components as available data, and assuming that the solenoidal and irrotational components of the flow differ from the two corresponding components of the compound Rankine model by a white Gaussian noise of variance σ^2, we get:

$$f_{so}(z) = \sum_{i=1}^{P}\Big(f_i(z) + a(z) + ib(z)\Big) \quad \text{and} \quad f_{ir}(z) = \sum_{j=1}^{N}\Big(f_j(z) + a(z) + ib(z)\Big)$$

with $a(z)$ and $b(z) \sim \mathcal{N}(0,\sigma^2)$. Function $f_{so} \triangleq u_{so} + iv_{so}$ (resp. $f_{ir} \triangleq u_{ir} + iv_{ir}$) is the complex representation of $\boldsymbol{w}_{so}$ (resp. of $\boldsymbol{w}_{ir}$), and P

and N denote respectively the number of vortices and sources/sinks of the flow. Their locations and number have been obtained by the technique described previously.

A maximum likelihood estimation of the Rankine model parameters leads to maximize with respect to the unknown parameters vector $\Theta \triangleq (r_\imath, \beta_\imath)_{\imath=1}^P \times (r_\jmath, \alpha_\jmath)_{\jmath=1}^N$ the following log-likelihood defined on the whole image domain Ω:

$$\mathcal{L}(\Theta) = \underbrace{\iint\limits_\Omega |f_{ir}(z) - \sum_\imath f_\imath(z)|^2 dz}_{\mathcal{L}_{so}} + \underbrace{\iint\limits_\Omega |f_{so}(z) - \sum_\jmath f_\jmath(z)|^2 dz}_{\mathcal{L}_{ir}} . \quad (28)$$

With the assumption that two circular linearity domains of the same nature do not intersect each other, the two solenoidal part of this expression can be expressed as, on a disk domain $\mathcal{D}_{so} = \bigcup_{\imath=1}^P \mathcal{D}_\imath$:

$$\begin{aligned} \mathcal{L}_{so}(\Theta) = \sum_{\imath=1}^P \iint\limits_{\mathcal{D}_\imath} |f_{so}(z) - h_\imath(r_\imath, z) - \sum_{k\neq\imath} g_k(z)|^2 dz \\ + \iint\limits_{\overline{\mathcal{D}}} |f_{so}(z) - \sum_{\imath=1}^P g_p(z)|^2 dz, \end{aligned} \quad (29)$$

where $\mathcal{D}_\imath$ denotes the disk associated to the $\imath$th singularity and $\overline{\mathcal{D}}_{so} \triangleq \Omega - \bigcup_{\imath=1}^P \mathcal{D}_\imath$. The irrotational part being obviously expressed in a very semilar way in considering a new non-overlapping disk domain $\mathcal{D}_{ir} = \bigcup_{\jmath=1}^N \mathcal{D}_\jmath$ and the adequate associated functions. It is important to remark that the non-overlapping assumption only apply to domains associated to singularities of the same type. Likelihood (29) is still valid for a vortex and a source combined in a swirl. For the sake of simplicity, we will develop the proposed method in the solenoidal case, and only give results of the irrotational part. They are indeed obtain in an exactly similar way.

To ensure that two singularity domains of the same type does not intersect each others, we have to consider an additional constraint whose rule is to hardly penalize the functional to be minimized, when assumptions of non intersecting circular domain are violated. Let us note this constraint $\mathcal{C}(r_\imath, r_\jmath)$ applied on any pair of singularity $(\imath, \jmath)$ with radius $(r_\imath, r_\jmath)$. The aim is now to find Θ that minimize $\mathcal{L}c_{so}(\Theta)$ such that:

$$\mathcal{L}c_{so}(\Theta) = \mathcal{L}_{so}(\Theta) + \sum_{(\imath,\jmath),\imath\neq\jmath} \mathcal{C}(r_\imath, r_\jmath) \quad (30)$$

where $(\imath, \jmath)$ indices any pair of singularity. Expanding this expression in the solenoidal case one gets:

$$\begin{aligned}\mathcal{L}c_{so}(\Theta) = &\sum_{\imath} \iint_{\mathcal{D}_\imath} \left\| \boldsymbol{\omega}_{so}(\boldsymbol{s}) + \frac{(\boldsymbol{s}-\boldsymbol{s}_\imath)^\perp}{r_\imath^2}\beta_\imath + \sum_{k\neq\imath} \frac{(\boldsymbol{s}-\boldsymbol{s}_k)^\perp}{\|\boldsymbol{s}-\boldsymbol{s}_k\|^2}\beta_k \right\|^2 d\boldsymbol{s} \\ &+ \iint_{\overline{\mathcal{D}}_\imath} \left\| \boldsymbol{\omega}_{so}(\boldsymbol{s}) + \sum_{k} \frac{(\boldsymbol{s}-\boldsymbol{s}_k)^\perp}{\|\boldsymbol{s}-\boldsymbol{s}_k\|^2}\beta_k \right\|^2 d\boldsymbol{s} + \sum_{(\imath,\jmath),\imath\neq\jmath} \mathcal{C}(r_\imath, r_\jmath)\end{aligned} \tag{31}$$

A minimizer of equation (31) is given by the resolution of $\boldsymbol{\nabla}\mathcal{L}c_{so} = 0$.

3.2.1. *Radius estimation*
Following the derivation developed in the appendix (49) we have:

$$\begin{aligned}\frac{\partial \mathcal{L}c_{so}(\Theta)}{\partial r_\imath} = &-4 \iint_{\mathcal{D}_\imath} \left[\boldsymbol{\omega}_{so}(\boldsymbol{s}) + \frac{(\boldsymbol{s}-\boldsymbol{s}_\imath)^\perp}{r_\imath^2}\beta_\imath + \sum_{k\neq\imath} \frac{(\boldsymbol{s}-\boldsymbol{s}_k)^\perp}{\|\boldsymbol{s}-\boldsymbol{s}_k\|^2}\beta_k \right] \cdot \frac{(\boldsymbol{s}-\boldsymbol{s}_\imath)^\perp}{r_\imath^3}\beta_\imath d\boldsymbol{s} \\ &+ \sum_{k\neq\imath} \frac{\partial \mathcal{C}(r_\imath, r_k)}{\partial r_\imath}.\end{aligned} \tag{32}$$

Then, the problem yields:

$$\begin{aligned}&\frac{\partial \mathcal{L}c_{so}(\Theta)}{\partial r_\imath} = 0 \\ \Leftrightarrow &4 \iint_{\mathcal{D}_\imath} \left[\boldsymbol{w}_{so}(x,y) \wedge (\boldsymbol{s}-\boldsymbol{s}_\imath) - (\boldsymbol{s}-\boldsymbol{s}_\imath) \cdot \sum_{k\neq\imath} \frac{(\boldsymbol{s}-\boldsymbol{s}_k)\beta_k}{\|\boldsymbol{s}-\boldsymbol{s}_k\|^2} \right] d\boldsymbol{s} - \iint_{\mathcal{D}_\imath} \frac{4\|\boldsymbol{s}-\boldsymbol{s}_\imath\|^2\beta_\imath}{r_\imath^2} d\boldsymbol{s} \\ &+ \frac{r_\imath^3}{\beta_\imath} \sum_{k\neq\imath} \frac{\partial \mathcal{C}(r_\imath, r_k)}{\partial r_\imath} = 0.\end{aligned} \tag{33}$$

Many solutions are available to solve this kind of non-linear equation, where the integration domain $\mathcal{D}_\imath$ depends on the unknown variable $r_\imath$ to estimate. We choose to use a fixed point iteration method. This kind of techniques consist in solving a problem of the form $x = g(x)$ given a previous iterate. The new problem read then $x^{(p+1)} = g(x^{(p)})$.

An iterative fixed point process may be written as:

$$
\begin{aligned}
&\frac{\partial \mathcal{L}c_{so}(\Theta)}{\partial r_\imath} = 0 \\
\Leftrightarrow & 4 \iint_{\mathcal{D}_\imath(p)} \left[\boldsymbol{w}_{so}(x,y) \wedge (\boldsymbol{s} - \boldsymbol{s}_\imath) - (\boldsymbol{s} - \boldsymbol{s}_\imath) \cdot \sum_{k \neq \imath} \frac{(\boldsymbol{s} - \boldsymbol{s}_k)\beta_k}{\|\boldsymbol{s} - \boldsymbol{s}_k\|^2} \right] d\boldsymbol{s} \\
& - \frac{4}{r_\imath^2(p+1)} \iint_{\mathcal{D}_\imath(p)} \|\boldsymbol{s} - \boldsymbol{s}_\imath\|^2 \beta_\imath d\boldsymbol{s} + \frac{r_\imath^3(p)}{\beta_\imath} \sum_{k \neq \imath} \frac{\partial \mathcal{C}(r_\imath(p), r_k)}{\partial r_\imath(p)} = 0.
\end{aligned}
\tag{34}
$$

which finally reads:

$$
r_\imath(p+1) = \sqrt{\frac{\mathcal{B}_\imath(p)}{\mathcal{A}_\imath(p) + \frac{r_\imath^3(p)}{\beta_\imath} \sum_{k \neq \imath} \frac{\partial \mathcal{C}(r_\imath(p), r_k)}{\partial r_\imath(p)}}},
\tag{35}
$$

with:

$$
\begin{cases}
\mathcal{A}_\imath(p) = 4 \displaystyle\iint_{\mathcal{D}_\imath(p)} \left[\boldsymbol{w}_{so}(x,y) \wedge (\boldsymbol{s} - \boldsymbol{s}_\imath) - (\boldsymbol{s} - \boldsymbol{s}_\imath) \cdot \sum_{k \neq \imath} \frac{(\boldsymbol{s} - \boldsymbol{s}_k)\beta_k}{\|\boldsymbol{s} - \boldsymbol{s}_k\|^2} \right] d\boldsymbol{s}, \\
\mathcal{B}_\imath(p) = 4 \displaystyle\iint_{\mathcal{D}_\imath(p)} \|\boldsymbol{s} - \boldsymbol{s}_\imath\|^2 \beta_\imath d\boldsymbol{s} = 2\pi r_\imath^4(p) \beta_\imath.
\end{cases}
\tag{36}
$$

Expressions $\mathcal{A}_\imath(p)$ and $\mathcal{B}_\imath(p)$ are computed directly from $\boldsymbol{w}_{so}$, $\boldsymbol{s}_\imath$,and $r_\imath^{(p)}$ and $\beta_\imath$ previously estimated.

3.2.1.1. *Choice of the constraint functional*

At that step, function $\mathcal{C}$ has to be defined. Such a function must have a low value if constraints are not violated (if in fact $(\mathrm{q}_{\imath\jmath} = r_\imath + r_\jmath - d_{\imath\jmath}) < 0$ where $d_{\imath\jmath}$ is the distance between centers $(\boldsymbol{s}_\imath, \boldsymbol{s}_\jmath)$) a high one in the other case (if $\mathrm{q}_{\imath\jmath} > 0$). It is common to employ, for that kind of problem, an approximation of the Heaviside function H associated with a very strong coefficient λ (in practice $\lambda = 10^{30}$). One can choose for instance the approximation proposed by Chan and Vese in [7]:

$$
\mathcal{C}(\mathrm{q}_{\imath\jmath}) = \lambda H_\epsilon(\mathrm{q}_{\imath\jmath}) = \frac{\lambda}{2}\Big(1 + \frac{2}{\pi}\mathrm{atan}(\frac{\mathrm{q}_{\imath\jmath}}{\epsilon})\Big).
\tag{37}
$$

The derivation of this function is an approximation of the Dirac function:

$$
\mathcal{C}'(\mathrm{q}_{\imath\jmath}) = \lambda \delta_\epsilon(\mathrm{q}_{\imath\jmath}) = \frac{\lambda}{\pi} \frac{\epsilon}{\epsilon^2 + \mathrm{q}_{\imath\jmath}^2}
\tag{38}
$$

Two graphics representations of these functions are shown in Figure 4 for different values of ϵ.

Such functions seem at first glance well adapted to our problem. As a matter of fact, starting from an admissible solution (non-overlapping disks), if the different radiuses growes slighty and continuously, the non-overlapping assumption is guarantee through function $\frac{\partial \mathcal{C}}{\partial r_\imath}$, who keep solutions into an admissible domain.

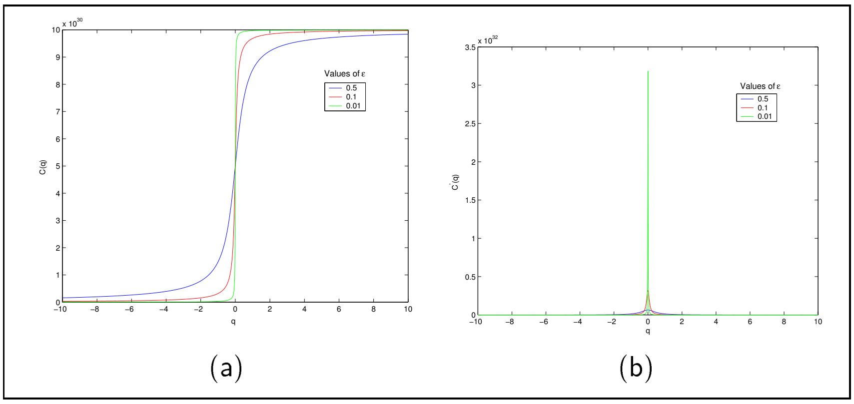

Figure 4. (a) *Graphic representation of a constraint defined as a strong Heaviside function and* (b) *its derivative for three different values of* ϵ

Nevertheless, in our case, within the fixed point strategy, the temporal evolution of $r_\imath(p)$ over iterations (p) is not necessary "continuous": the difference $r_\imath(p+1) - r_\imath(p)$ can be important. As a consequence, if $r_\imath(p)$ respects the constraint, it is possible (if the evolution is too violent) for $r_\imath(p+1)$ to have its value in the domain where constraints are violated. In that case, following relations (35) and (38), the contribution of $\frac{\partial \mathcal{C}}{\partial r_\imath}$ in the estimation of the radius is neglected, since this constraint is effective only at the frontier of the admissible domain. The "barrier" imposed at the frontier to prevent from overlapping has been crossed and $\frac{\partial \mathcal{C}}{\partial r_\imath}$ has no effects.

To cope with this particular phenomenon, we have to find a function whose derivative become "active" (*i.e.* with very strong values) not only at the frontier of two domains, but all over the non desired area. Instead of using (37), we preferred to use for $\mathcal{C}$:

$$\mathcal{C}(\mathrm{q}_{\imath\jmath}) = \lambda \mathrm{q}_{\imath\jmath} H_\epsilon(\mathrm{q}_{\imath\jmath}), \tag{39}$$

whose derivative is:

$$\mathcal{C}'(\mathrm{q}_{\imath\jmath}) = \frac{\partial \mathcal{C}(\mathrm{q}_{\imath\jmath})}{\partial r_\imath} = \lambda \Big(H_\epsilon(\mathrm{q}_{\imath\jmath}) + \mathrm{q}_{\imath\jmath} \delta_\epsilon(\mathrm{q}_{\imath\jmath}) \Big).$$

Graphics representations of $\mathcal{C}$ and $\mathcal{C}'$ can be shown on Figure 5. In that case, $\mathcal{C}'$ is "active" not only at the frontier of two domains but also over the whole area where $r_\imath(p+1)$ is not valid.

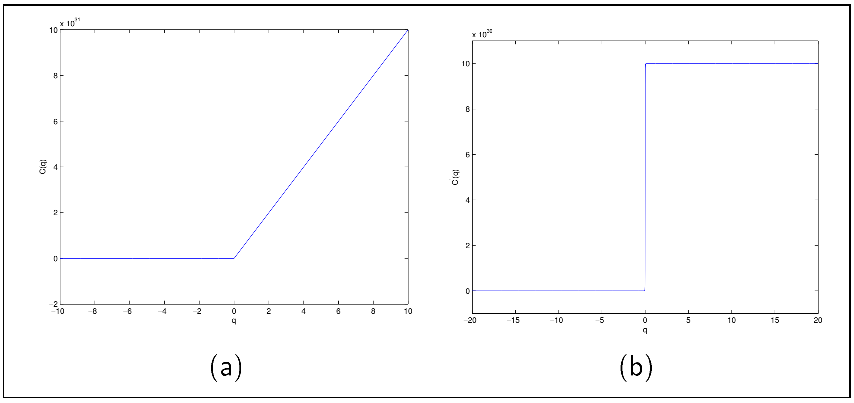

Figure 5. (a) *Graphic representation of our proposed constraint and* (b) *its derivative for* $\epsilon = 0.01$

3.2.2. *Strengths parameters estimation*
In that simpler case, the partial derivative with respect to one of the $\beta_\imath$'s is:

$$\begin{aligned}\frac{\partial \mathcal{L}c_{so}(\Theta)}{\partial \beta_\imath} &= 2\iint_{\mathcal{D}_\imath}\left[\boldsymbol{\omega}_{so}(\boldsymbol{s}) + \frac{(\boldsymbol{s}-\boldsymbol{s}_\imath)^\perp}{r_\imath^2}\beta_\imath + \sum_{k\neq\imath}\frac{(\boldsymbol{s}-\boldsymbol{s}_k)^\perp}{\|\boldsymbol{s}-\boldsymbol{s}_k\|^2}\beta_k\right]\cdot\frac{(\boldsymbol{s}-\boldsymbol{s}_\imath)^\perp}{r_\imath^2}d\boldsymbol{s} \\ &+ 2\iint_{\overline{\mathcal{D}}}\left[\boldsymbol{\omega}_{so}(\boldsymbol{s}) + \sum_{k}\frac{(\boldsymbol{s}-\boldsymbol{s}_k)^\perp}{\|\boldsymbol{s}-\boldsymbol{s}_k\|^2}\beta_k\right]\cdot\frac{(\boldsymbol{s}-\boldsymbol{s}_\imath)^\perp}{\|\boldsymbol{s}-\boldsymbol{s}_\imath\|^2}d\boldsymbol{s} \\ &+ 2\sum_{k\neq\imath}\iint_{\mathcal{D}_k}\left[\boldsymbol{\omega}_{so}(\boldsymbol{s}) + \frac{(\boldsymbol{s}-\boldsymbol{s}_k)^\perp}{r_k^2}\beta_k + \sum_{p\notin\{k,\imath\}}\frac{(\boldsymbol{s}-\boldsymbol{s}_p)^\perp}{\|\boldsymbol{s}-\boldsymbol{s}_p\|^2}\beta_p\right]\cdot\frac{(\boldsymbol{s}-\boldsymbol{s}_\imath)^\perp}{\|\boldsymbol{s}-\boldsymbol{s}_\imath\|^2}d\boldsymbol{s}.\end{aligned} \tag{40}$$

Then:

$$
\begin{aligned}
&\frac{\partial \mathcal{L}_{so}(\Theta)}{\partial \beta_\imath} = 0 \\
&\Leftrightarrow -\frac{\beta_\imath}{\hat{r}_\imath^4} \underbrace{\iint\limits_{\mathcal{D}_\imath} \|\boldsymbol{s}-\boldsymbol{s}_\imath\|^2 d\boldsymbol{s}}_{\frac{\pi}{2}\hat{r}_\imath^4} + \frac{1}{\hat{r}_\imath^2} \underbrace{\iint\limits_{\mathcal{D}_\imath} \left[(\boldsymbol{\omega}_{so}(\boldsymbol{s}) + \sum_{k\neq\imath} \frac{(\boldsymbol{s}-\boldsymbol{s}_k)^\perp}{\|\boldsymbol{s}-\boldsymbol{s}_k\|^2}\beta_k) \cdot (\boldsymbol{s}-\boldsymbol{s}_\imath)^\perp \right] d\boldsymbol{s}}_{\frac{\pi}{2}\hat{r}_\imath^2 \text{ according to (35-36)}^1} \\
&\quad - \beta_\imath \underbrace{\Big(\iint\limits_{\overline{\mathcal{D}}} \frac{1}{\|\boldsymbol{s}-\boldsymbol{s}_\imath\|^2} d\boldsymbol{s} + \sum_{k\neq\imath} \iint\limits_{\mathcal{D}_k} \frac{1}{\|\boldsymbol{s}-\boldsymbol{s}_k\|^2} d\boldsymbol{s} \Big)}_{A} \\
&\quad + \underbrace{\iint\limits_{\overline{\mathcal{D}}} \left[\boldsymbol{\omega}_{so}(\boldsymbol{s}) + \sum_{k\neq\imath} \frac{(\boldsymbol{s}-\boldsymbol{s}_k)^\perp}{\|\boldsymbol{s}-\boldsymbol{s}_k\|^2}\beta_k \right] \cdot \frac{(\boldsymbol{s}-\boldsymbol{s}_\imath)^\perp}{\|\boldsymbol{s}-\boldsymbol{s}_\imath\|^2} d\boldsymbol{s}}_{B} \\
&\quad + \underbrace{\sum_{k\neq\imath} \iint\limits_{\mathcal{D}_k} \left[\boldsymbol{\omega}_{so}(\boldsymbol{s}) + \frac{(\boldsymbol{s}-\boldsymbol{s}_k)^\perp}{r_k^2}\beta_k + \sum_{p\notin\{k,\imath\}} \frac{(\boldsymbol{s}-\boldsymbol{s}_p)^\perp}{\|\boldsymbol{s}-\boldsymbol{s}_p\|^2}\beta_p \right] \cdot \frac{(\boldsymbol{s}-\boldsymbol{s}_\imath)^\perp}{\|\boldsymbol{s}-\boldsymbol{s}_\imath\|^2}}_{C} = 0 \\
&\Leftrightarrow \beta_\imath = \frac{B+C}{A}, \text{with} \quad A = \iint\limits_{\Omega-\mathcal{D}_\imath} \frac{1}{\|\boldsymbol{s}-\boldsymbol{s}_\imath\|^2} d\boldsymbol{s}
\end{aligned}
\tag{41}
$$

At this step, A, B, and C are directly computed from given observations $\boldsymbol{w}_{so}$, $\boldsymbol{s}_\imath$ and previous estimated radiuses $r_\imath$ and strengths $\beta_\imath$.

3.2.3. *Irrotational case*

In a similar way, the optimal singularity radius is given by:

$$
r_\imath^{(p+1)} = \sqrt{\frac{\mathcal{B}_\imath^{(p)}}{\mathcal{A}_\imath^{(p)} + \frac{r_\imath^{3(p)}}{\alpha_\imath} \sum_{k\neq\imath} \mathcal{C}'(r_\imath^{(p)}, r_k)}}, \tag{42}
$$

with:

$$
\begin{cases}
\mathcal{A}_\imath^{(p)} = 4 \iint\limits_{\mathcal{D}_\imath^{(p)}} \left[\boldsymbol{w}_{ir}(x,y) \cdot (\boldsymbol{s} - \boldsymbol{s}_\imath) - (\boldsymbol{s} - \boldsymbol{s}_\imath) \cdot \sum_{k \neq \imath} \frac{(\boldsymbol{s} - \boldsymbol{s}_k)\alpha_k}{\|\boldsymbol{s} - \boldsymbol{s}_k\|^2} \right] d\boldsymbol{s}, \\
\mathcal{B}_\imath^{(p)} = 4 \iint\limits_{\mathcal{D}_\imath^{(p)}} \|\boldsymbol{s} - \boldsymbol{s}_\imath\|^2 \alpha_\imath d\boldsymbol{s} = 2\pi r_\imath^{4(p)} \alpha_\imath.
\end{cases}
\tag{43}
$$

The optimal strength source/sink , $\alpha_\jmath$, is given by $\alpha_\jmath = \frac{B+C}{A}$ with:

$$
B = \iint\limits_{\overline{\mathcal{D}}} \left[\boldsymbol{\omega}_{ir}(\boldsymbol{s}) - \sum_{k \neq \jmath} \frac{(\boldsymbol{s} - \boldsymbol{s}_k)}{\|\boldsymbol{s} - \boldsymbol{s}_k\|^2} \alpha_k \right] \cdot \frac{(\boldsymbol{s} - \boldsymbol{s}_\jmath)}{\|\boldsymbol{s} - \boldsymbol{s}_\jmath\|^2} d\boldsymbol{s}, \tag{44}
$$

and

$$
C = \sum_{k \neq \jmath} \iint\limits_{\mathcal{D}_k} \left[\boldsymbol{\omega}_{ir}(\boldsymbol{s}) - \frac{(\boldsymbol{s} - \boldsymbol{s}_k)}{r_k^2} \alpha_k - \sum_{p \notin \{k,\jmath\}} \frac{(\boldsymbol{s} - \boldsymbol{s}_p)}{\|\boldsymbol{s} - \boldsymbol{s}_p\|^2} \alpha_p \right] \cdot \frac{(\boldsymbol{s} - \boldsymbol{s}_\jmath)}{\|\boldsymbol{s} - \boldsymbol{s}_\jmath\|^2} d\boldsymbol{s}. \tag{45}
$$

Let us remark that in both cases the term A is the same. Through Green theorem this term can be computed from the contour of domain $\Omega - \mathcal{D}_\imath$. Green theorem states that for any continuously differentiable vector field $\boldsymbol{\omega} \triangleq (p,q)$ on a planar region Ω we have:

$$
\iint\limits_{\Omega} \left(\frac{\partial q}{\partial y} - \frac{\partial p}{\partial x} dx dy \right) = \int\limits_{\partial\Omega} p(x,y)dx + q(x,y)dy.
$$

In our case let us pose:

$$
\frac{\partial q(x,y)}{\partial y} = \frac{1}{2(x^2+y^2)} \qquad \text{with} \qquad q(x,y) = \frac{1}{2x} \arctan \frac{y}{x} \qquad \text{and}
$$

$$
\frac{\partial p(x,y)}{\partial x} = -\frac{1}{2(x^2+y^2)} \qquad \text{with} \qquad p(x,y) = -\frac{1}{2y} \arctan \frac{x}{y}
$$

we have then:

$$
\iint\limits_{\Omega} \frac{1}{x^2+y^2} dx dy = \frac{1}{2} \int\limits_{\partial\Omega} -\frac{1}{y} \arctan \frac{x}{y} dx + \frac{1}{x} \arctan \frac{y}{x} dy.
$$

The right hand side expression is then much cheaper to compute numerically.

3.3. Method summary

Before turning to the experimental results, and in order to give a clear view of the different treatments involved by our method, let us summarize the overall proposed technique for extracting the vortices, sinks and sources from a given velocity field, and estimating the associated Rankine models.

For a given dense velocity field, $\boldsymbol{\omega}$, we first separate through a 2D Fourier transform the two solenoidal and irrotational components (13-14). From these components, the stream function ψ and of the velocity potential ϕ are obtained through the numerical integrations of (15). The search for the local maxima of functions ϕ^2 and ψ^2 gives us the location of the different vortices and sinks/sources. To make this step robust, this maxima extraction – which is obtained in practice through simple morphological processing of the potential functions– we consider the Bhattacharyya distance between two multidimensional Gaussian laws [5]:

$$d_B[\mathcal{N}_1(\boldsymbol{\mu_1}, \Sigma_1), \mathcal{N}_2(\boldsymbol{\mu_2}, \Sigma_2)] = \frac{1}{4}(\boldsymbol{\mu_2} - \boldsymbol{\mu_1})^T(\Sigma_1 + \Sigma_2)^{-1}(\boldsymbol{\mu_2} - \boldsymbol{\mu_1}) + \frac{1}{2}\ln(\frac{\det(\Sigma_2 + \Sigma_1)}{2\sqrt{\det(\Sigma_1 \Sigma_2)}}). \tag{46}$$

For each component (*i.e.*, the irrotational one or the solenoidal one) we compute this distance for the two Gaussian distributions corresponding to the error between the considered Rankine model for two consecutive numbers of singularities and the known corresponding component of the flow. For instance for the solenoidal component, we compute: $d_B[\mathcal{N}_1(\boldsymbol{\omega}_{so} - \boldsymbol{\omega}^n_{\Theta_{so}}), \mathcal{N}_2(\boldsymbol{\omega}_{so} - \boldsymbol{\omega}^{n+1}_{\Theta_{so}}]$ where the field $\boldsymbol{\omega}^n_{\Theta_{so}}$ correspond to a maximum likelihood estimate of Rankine model with n vortices (35-45). Starting with no singularities, we increase successively the number of singularities by considering the highest local maxima of its corresponding squared potential function. When the Bhattacharyya distance between two consecutive models is small enough (*i.e.*, when the introduction of a new singularity does not bring additional information) the process is stopped.

A schematic view of the complete method is as follows:

$\boldsymbol{\omega}$

- Compute $\boldsymbol{\omega}_{ir}$
- Compute velocity potential ϕ
- Set $n = 0$, $\boldsymbol{\omega}^0_{\Theta_{ir}} = 0$
- Select the $n+1$ highest maxima of ϕ^2
- Estimate Rankine irrotational flow: $\boldsymbol{\omega}^{n+1}_{\Theta_{ir}}$
- Compute: $d^n_B[\mathcal{N}_1(\boldsymbol{\omega}_{ir} - \boldsymbol{\omega}^n_{\Theta_{ir}}), \mathcal{N}_2(\boldsymbol{\omega}_{ir} - \boldsymbol{\omega}^{n+1}_{\Theta_{ir}})]$
- If $(d^n_B) > 0.01$ $n = n+1$

else

- Compute $\boldsymbol{\omega}_{so}$
- Compute stream function ψ
- Set $n = 0$, $\boldsymbol{\omega}^0_{\Theta_{so}} = 0$
- Select the $n+1$ highest maxima of ψ^2
- Estimate Rankine solenoidal flow: $\boldsymbol{\omega}^{n+1}_{\Theta_{so}}$
- Compute: $d^n_B[\mathcal{N}_1(\boldsymbol{\omega}_{so} - \boldsymbol{\omega}^n_{\Theta_{so}}), \mathcal{N}_2(\boldsymbol{\omega}_{so} - \boldsymbol{\omega}^{n+1}_{\Theta_{so}})]$
- If $(d^n_B) > 0.01$ $n = n+1$

else

$$\boldsymbol{\omega}_{\Theta} = \boldsymbol{\omega}_{\Theta_{ir}} + \boldsymbol{\omega}_{\Theta_{so}} \tag{47}$$

4. Experimental results

In this section we present some experimental results to evaluate our method. The experiments have been carried out both on a synthetic benchmark and on three different real examples. In order to show the accuracy of the proposed method we present first the results obtained on a synthetic motion field.

4.1. Synthetic example

The synthetic example we consider to assess the performance of our method arises from a Rankine model involving four vortices, one sink, and one source. The set of parameters used to obtain the flow are

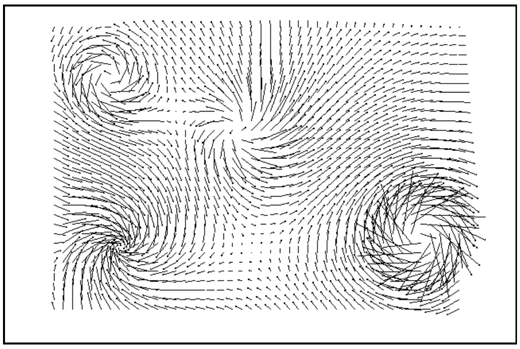

Figure 6. Synthetic Rankine motion field associated to the parameters of table I.

gathered in the left part of table I. The associated velocity field is presented in figure 6.

The results are reported in the right part of table I. They have been obtained on a noisy version of the synthetic motion field[2]. For each singularity the parameters are well recovered (locations, radius, strength). In order to assess the quality of the reconstructed motion field, we can quantify its global agreement with the initial motion field through the angular discrepancy criterion proposed by Barron *et al.* [4]. We get an average angular error of 0.40° with a standard deviation of 0.38° between the true velocity field and the reconstructed one.

Table I. Estimation of Rankine models on the synthetic field of Fig. 6

	Synthetic parameters			Estimated parameters			Error on strength
	location	radius	strength	location	radius	strength	
Source	$(210, 60)$	20	250.0	$(211, 60)$	21	249.6	0.16%
Sink	$(100, 180)$	30	-150.0	$(100, 180)$	30	-151.5	1.0%
Vortex	$(200, 350)$	15	-400.0	$(201, 350)$	15	-399.1	0.22%
Vortex	$(210, 60)$	50	-250.0	$(211, 60)$	39	-247.9	0.84%
Vortex	$(50, 50)$	20	200.0	$(50, 49)$	20	205.3	2.65%
Vortex	$(100, 180)$	25	150.0	$(101, 180)$	26	149.8	0.13%

For this synthetic example, we present in figure 7 the two solenoidal and irrotational components that have been extracted from the initial

[2] Each component of the velocity field has been corrupted by a centered Gaussian noise ($\sigma = 0.9$)

velocity field. The estimated stream function and velocity potential and their associated squared functions are also presented in the second and third rows of the same figure. In the last row of figure 7 we superimposed to the solenoidal and irrotational components the estimated singularity domains.

The time computation for the whole process (field separation, singular point detection and Rankine model identification) for this synthetic example is $t = 119s$, on a Sun Ultra 10 (with a c.p.u rate at 440 Mhz), the image size being (396x276) pixels. It is important to note that most of this computation time is due to the motion field decomposition in the Fourier domain (the time needed, under a Matlab environment, for this decomposition is $t = 72s$ which is $60,5\%$ of the global computational time).

4.2. Real motion fields

We show here three results obtained on real velocity fields. The velocity fields have been estimated with a motion estimator dedicated to fluid images [10]. As mentioned previously, the corresponding laminar component is estimated through the same technique, with a smoothness term enforcing a null divergence and curl prior. The laminar component enables to fix the boundary conditions. Indeed, removing this global transport component from the flow under consideration then makes reasonable the assumption of vanishing at infinity.

The first example corresponds to the motion between two consecutive images of the infra-red channel of Meteosat, shot the 21^{st} of January 1998. An image of the sequence is shown in figure 8(a). It exhibits a large trough of low pressure (lower left part of the image) together with a large cloud structure moving in the upper right part of the image. The corresponding vector field with its laminar component removed is visible in figure 8(b).

The two solenoidal and irrotational components of this velocity field are shown in the first row of figure (9). The stream lines and the level curves of the velocity potential are presented in the second row of the same figure, whereas the squared potential functions are plotted in the third row. The last row of figure (9) presents the estimated singularity domains. The corresponding parametric velocity field is visible in figure 8c.

Due to the restricted form of the parametric model (let us recall that the Rankine model is one of the simplest vortex model), the reconstructed velocity field deviates slighty from the real one. The global discrepancy, following criterion of Barron *et al.* [4], is $4.71_{o} \pm 2.18_{o}$. Considering this discrepancy measure, we see that main characteristics

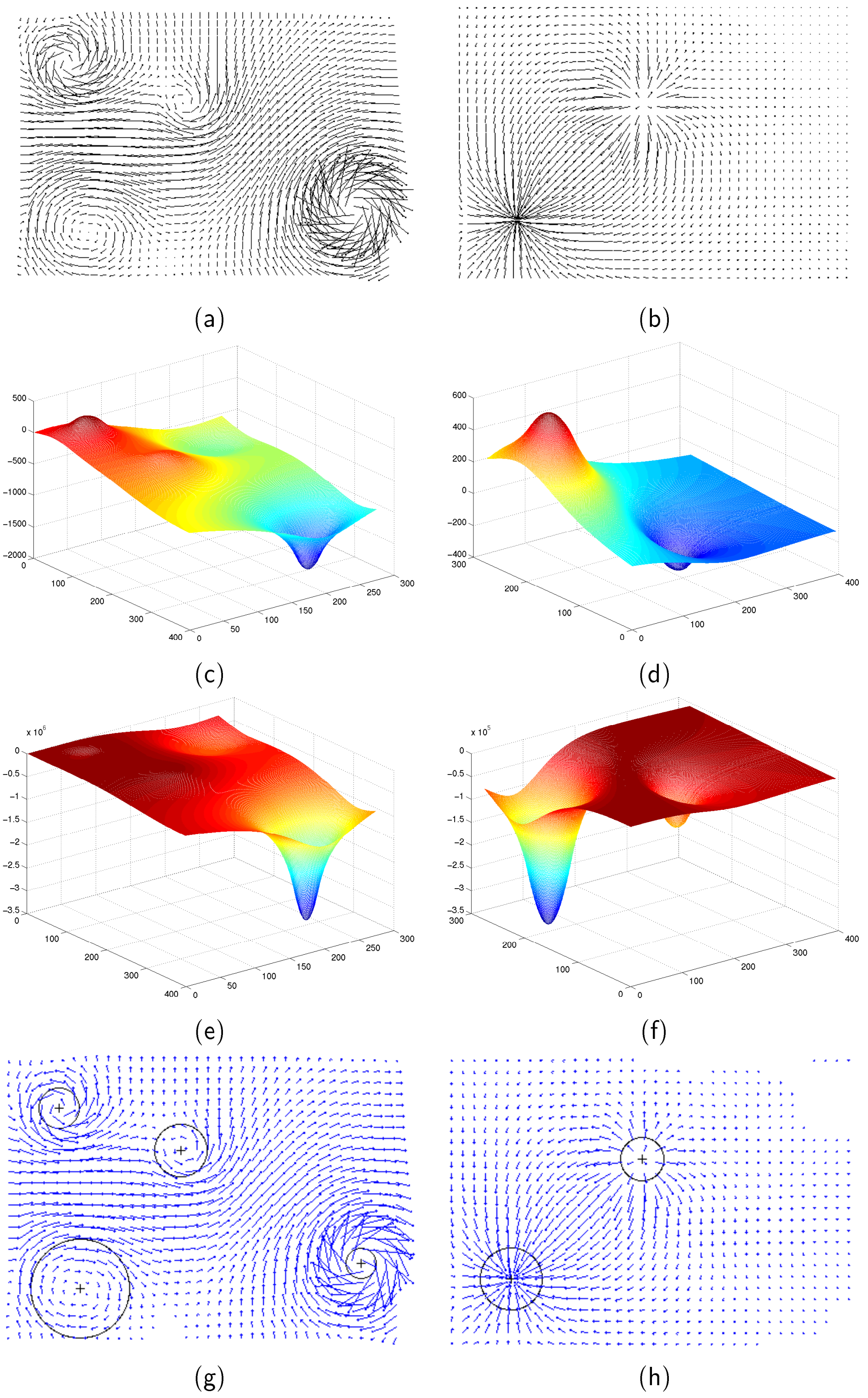

Figure 7. Results on the synthetic motion field of figure 6 – (a) solenoidal and (b) irrotational part of the motion field; (c) stream function and (d) velocity potential; (e) squared stream function and (f) squared velocity potential and (g,h) the singularities and their associated domains of linearity superimposed to the corresponding motion field.

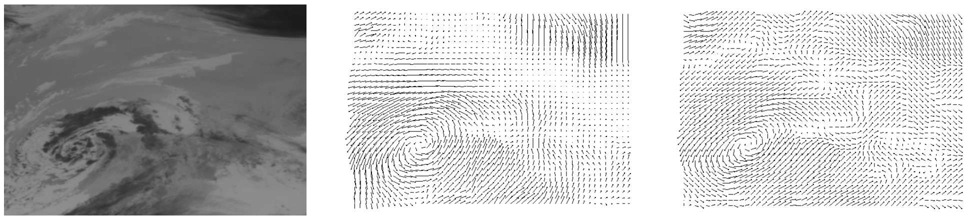

Figure 8. (a): Infrared Meteosat image; (b): dense velocity field; (c): parametric Rankine flow.

features of the motion we have extracted (singular points and radiuses of their associated linear domains) allows to get a good parametric description of the flow. The global time computation for this example is $t = 270s$ on a Sun Ultra 10 (440 Mhz), the image size being (396x276) pixels.

The second real example we present corresponds to water vapor Meteosat images, acquired the 4^{th} of August 1995. This sequence represents a depression in the left part of the imaged area and a convective cell in the center of the image. An image of the sequence and the associated motion field can be seen on figures 11 (a,b) respectively.

For this motion field we present figure 10 the same kind of results as in the previous example. The associated reconstructed parametric Rankine flow is presented in figure 11. Again, This flow captures well the main visible structures (four vortices and one source). The method as it stands is not able to locate, even roughly singularities which lie outside the image plane. The consequence of this can be observed in the reconstructed field: whereas the irrotational component in Fig. 10(b) strongly suggests the presence of one or two singularities, on the left, outside the image plane the estimated parametric Rankine flow does not capture them, which limits the accuracy of the reconstruction.

The global discrepancy between the true and the reconstruct motion field, following [4], is $6.46^{\circ} \pm 4.64^{\circ}$. The global time computation is $t = 121s$ on a Sun Ultra 10 (440 Mhz), for a (512x256) image. We can remark that whereas the image size is grether than in previous example, the computation time required is lower. This is due to a lower number of singularities detected. The time computation depends more on the number of singularities than on the image size.

The last velocity field corresponds to an infrared Meteosat sequence, acquired the 4^{th} of August 1995. It represents the explosion of active convective cells. These cells are associated to high vertical motion. They are therefore the center of highly diverging area within the 2D apparent

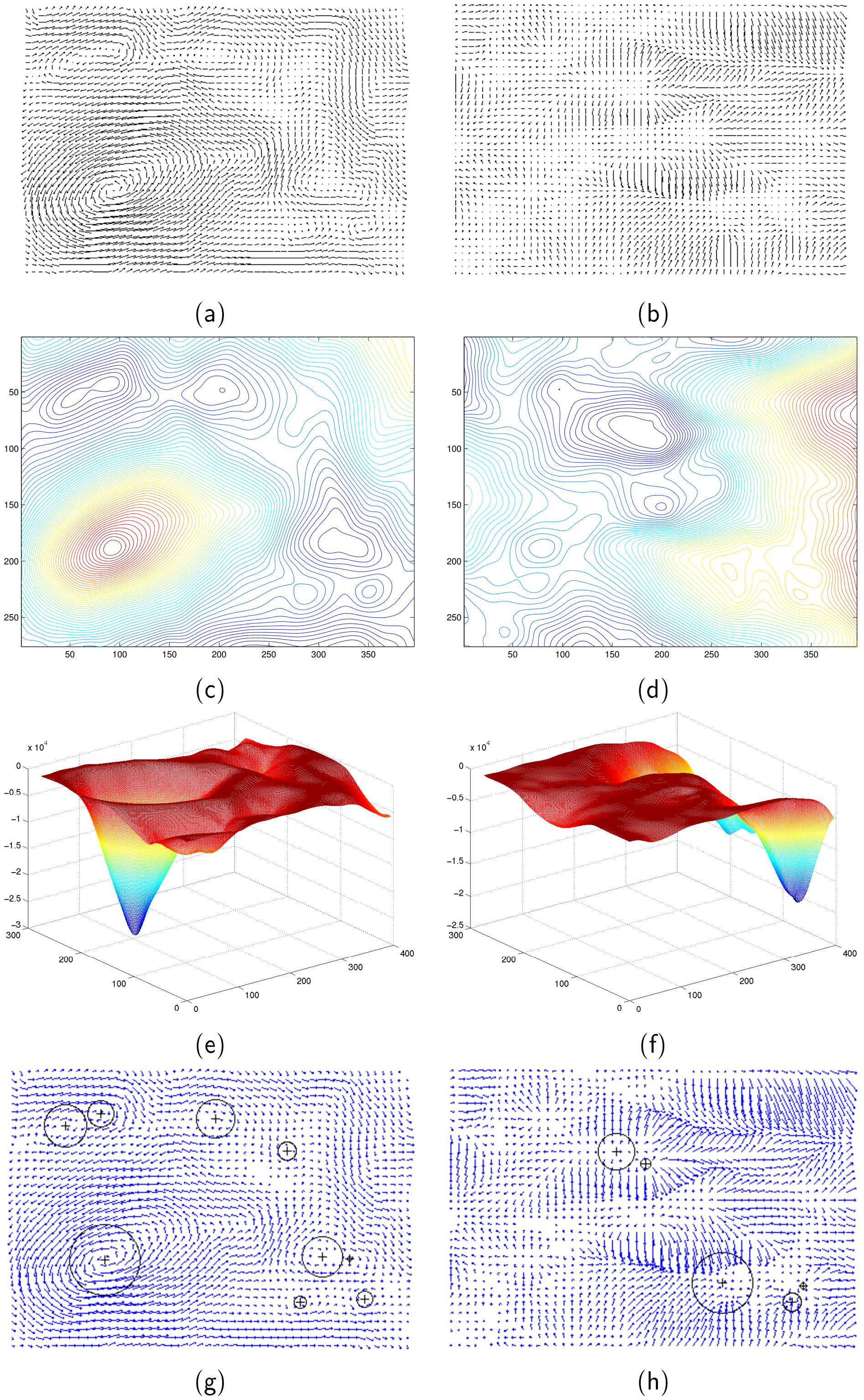

Figure 9. Results on the motion field presented figure 8 – (a) solenoidal and (b) irrotational parts of the motion field; (c) streamlines and (d) level curves of the velocity potential ; (e) squared stream function and (f) squared velocity potential ; estimated singularities superimposed on the corresponding component of the velocity field: vortices (g) and sinks/sources (h)

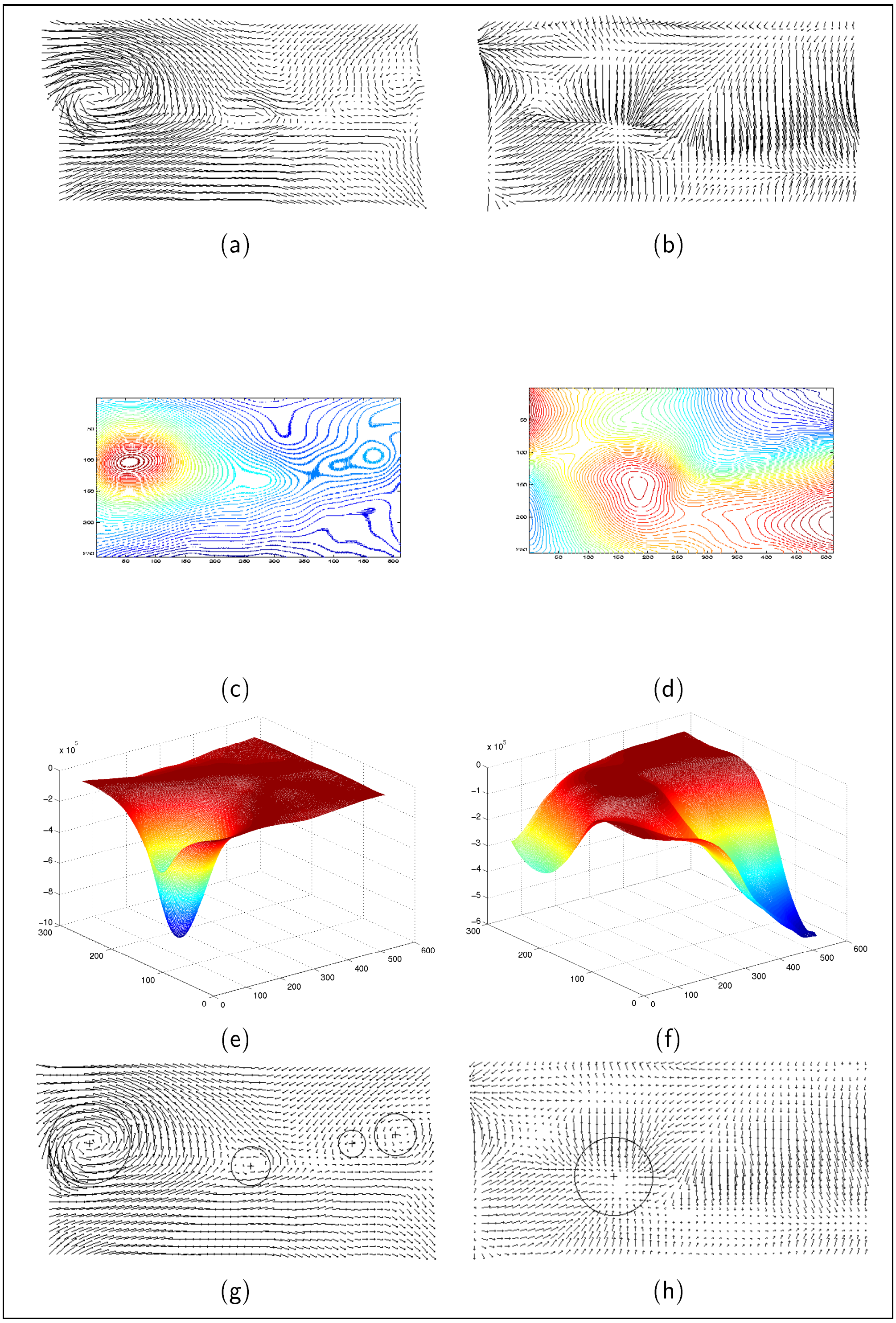

Figure 10. Results on the motion field presented figure 11 – (a) solenoidal and (b) irrotational parts of the motion field; (c) streamlines and (d) level curves of the velocity potential ; (e) squared stream function and (f) squared velocity potential ; estimated singularities: vortices (g) and sinks/sources (h)

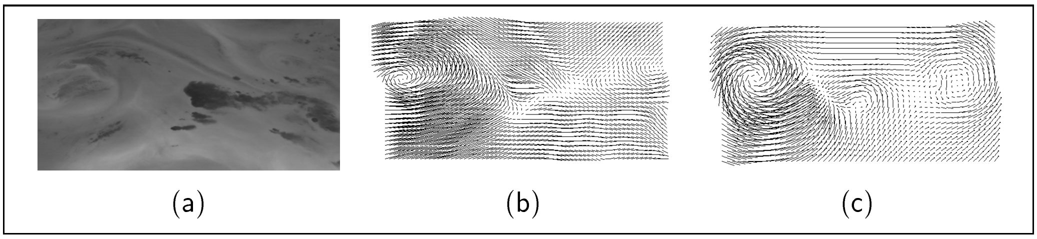

Figure 11. (a): Water vapor Meteosat image; (b): dense velocity field ; (c): parametric Rankine flow.

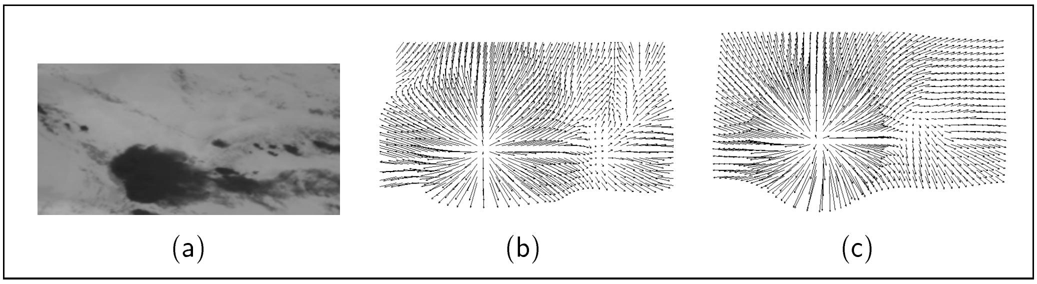

Figure 12. (a): Infrared Meteosat image; (b): dense velocity field; (c): parametric Rankine flow.

motion field. An image of the sequence and the associated dense motion field are shown on figures 12 (a,b).

Figure 13 presents the results obtained for this example. As we can see, the two main convective cells are very well captured. We have also extracted different vortices accounting for secondary motions of the cells present in the image. The corresponding reconstructed parametric field is also shown figure 12.

The global discrepancy between the true and the reconstruct motion field is $5.62^o \pm 2.15^o$. Again, despite the simplicity of the model used, the global parametric description of the flow allows to represent in a compact but informative way the original dense motion field. The global computation time is $t = 48s$ on a Sun Ultra 10 (440 Mhz), for a (256x128) image.

4.3. Comparison with winding numbers technique

Other techniques are available to extract singular points from a dense motion field. One of the most popular is based on the use of Poincaré indices also called winding numbers. The winding number (or index) of a closed curve in a vector field amounts to the numbers of turns, $\frac{1}{2\pi}\int d(\tan^{-1} u/v)$, that the field undergoes along the curve. Its value is $+1$ if the considered Jordan curve surrounds a vortex/sink/source

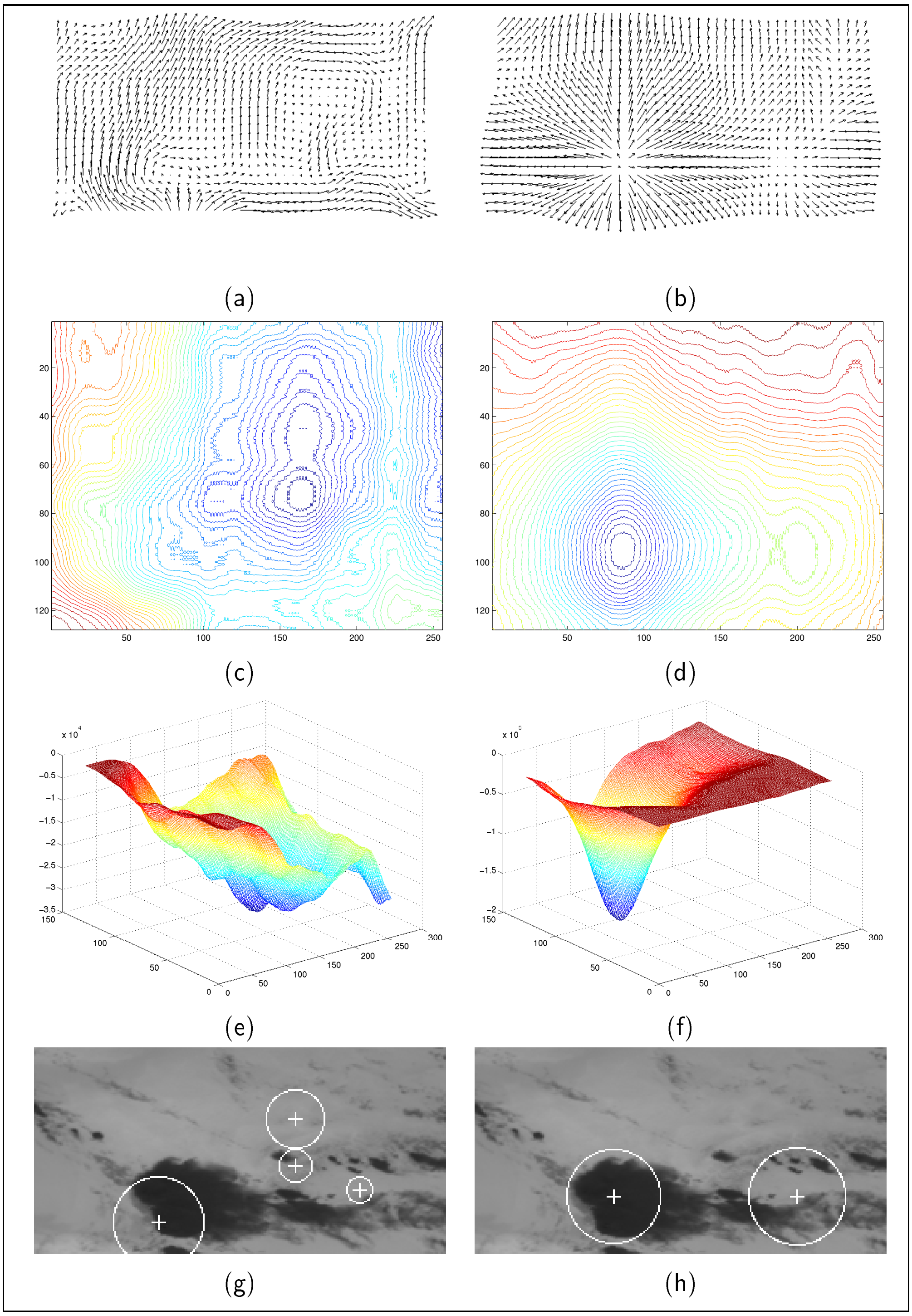

Figure 13. Results on the motion field presented figure 12 - (a) solenoidal and (b) irrotational parts of the motion field; (c) streamlines and (d) level curves of the velocity potential ; (e) squared stream function and (f) squared velocity potential ; estimated singularities: vortices (g) and sinks/sources (h).

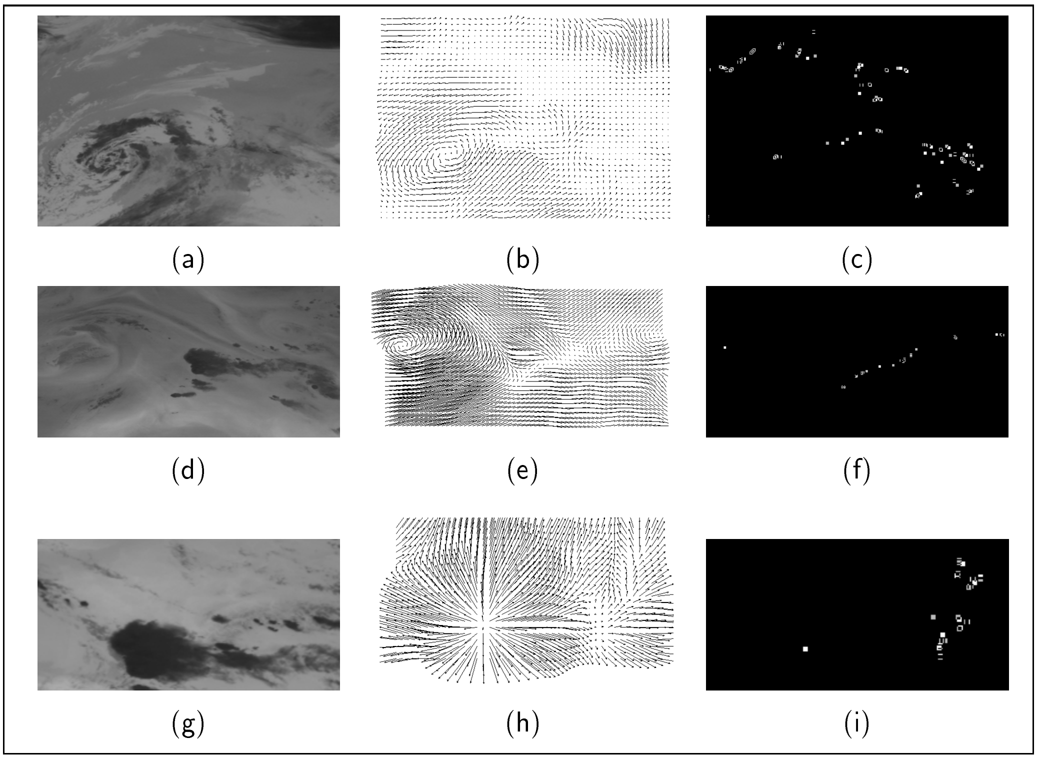

Figure 14. (a,d,g): Original real Meteosat images; ; (b,e,h): associated dense motion fields; (c,f,i): blobs of singularities estimated with winding numbers.

[8, 21, 30]. In practice, due to the image discretization, a small blob (whose size depends on the size of used curve) of +1 index pixels is obtained in the neighborhood of a singular point.

This method as the advantage to be fast. Nevertheless, it remains based on a local criterion which is not robust to noise. Furthermore, only blobs containing a potential singular point may be detected with such technique; the concerned point has then to be extracted from such blobs with other adhoc techniques.

In order to visualize the difference between such an approach and the one we propose, we present, in figure 14, for the three real motion fields, the different blobs detected with winding index.

We can note that the correct singular points are always detected. Nevertheless, the results are cluttered by a large number of false positive due to the sensitivity of the technique. Those spurious points have then to be removed with some post-processing treatments.

5. Conclusion

We have proposed an original technique to detect singular points and their associated domain of linearity from dense motion fields measured in image sequences. This technique is based on the decomposition of the motion field in terms of its irrotational and solenoidal components. From these components, we extract by integration the associated stream function and the velocity potential, whose local extrema provide the location of vortices and sinks/sources. The strength and linearity domain associated to each of these detected singular points are then obtained from a maximum likelihood estimation of a parametric Rankine model.

This method has been validated on synthetic and real examples, and has proved to extract the main structures of a motion field. Compared to an usual winding number technique, our approach is more robust to various sources of noise.

As a by product, the approach provides a simple way to extract streamlines, velocity potential, solenoidal or irrotational components, which are central to most studies of fluids.

As a final remark let us outline that the method described here is fast and requires no tuning of parameters.

Acknowledgements

The authors would like to thank Bernard Delyon from the IRMAR laboratory of university of Rennes I for valuable comments on this work.

References

1. R. Adrian. Particle imaging techniques for experimental fluid mechanics. *Annal Rev. Fluid Mech.*, 23:261–304, 1991.
2. V.I. Arnold. Ordinary differential equations. MIT Press, 1990.
3. L. Bannehr, R. Rohn, and G. Warnecke. A functionnal analytic method to derive displacement vector fields from satellite image sequences. *Int. Journ. of Remote Sensing*, 17(2):383–392, 1996.
4. J. Barron, D. Fleet, and S. Beauchemin. Performance of optical flow techniques. *Int. J. Computer Vision*, 12(1):43–77, 1994.
5. M. Basseville. Distance measure for signal processing and pattern recognition. *Signal Processing*, 18:349–369, 1989.
6. D. Béréziat, I. Herlin, and L. Younes. A generalized optical flow constraint and its physical interpretation. In *Proc. Conf. Comp. Vision Pattern Rec.*, volume 2, pages 487–492, Hilton Head Island, South Carolina, USA, 2000.

7. F. Chan and L.-A. Vese. Active contours without edges. *IEEE Trans on Image Processing*, 10(2):266–277, February 2001.
8. I. Cohen and I. Herlin. Optical flow and phase portrait methods for environmental satellite image sequences. In *Proc. 4th Europ. Conf. Computer Vision*, volume 2, pages 141–150, Cambridge, UK, Apr 1996.
9. I. Cohen and I. Herlin. Non uniform multiresolution method for optical flow and phase portrait models: Environmental applications. *Int. J. Computer Vision*, 33(1):29–49, 1999.
10. T. Corpetti, E. Mémin, and P. Pérez. Dense estimation of fluide flows. *IEEE Trans on Pattern Analysis and Machine Intelligence*, 24(3), March 2002.
11. S. Das Peddada and R. McDevitt. Least average residual algorithm (LARA) for tracking the motion of arctic sea ice. *IEEE trans. on Geoscience and Remote sensing*, 34(4):915–926, 1996.
12. J.M. Fitzpatrick. A method for calculating velocity in time dependent images based on the continuity equation. In *Proc. Conf. Comp. Vision Pattern Rec.*, pages 78–81, San Francisco, USA, 1985.
13. J.M. Fitzpatrick and C.A. Pederson. A method for calculating fluid flow in time dependant density images. *Electronic Imaging*, 1:347–352, 1988.
14. R.M. Ford. Critical point detection in fluid flow images using dynamical system properties. *Pattern Recognition*, 30(12):1991–2000, 1997.
15. R.M. Ford and R. Strickland. Representing and visualizing fluid flow images and velocimetry data by nonlinear dynamical systems. *Graph. Mod. Image Proc.*, 57(6):462–482, 1995.
16. R.M. Ford, R. Strickland, and B. Thomas. Image models for 2D flow visualization and compression. *Graph. Mod. Image Proc.*, 56(1):75–93, 1994.
17. B. Horn and B. Schunck. Determining optical flow. *Artificial Intelligence*, 17:185–203, 1981.
18. R. Larsen, K. Conradsen, and B.K. Ersboll. Estimation of dense image flow fields in fluids. *IEEE trans. on Geoscience and Remote sensing*, 36(1):256–264, 1998.
19. M. Maurizot, P. Bouthemy, and B. Delyon. 2D fluid motion analysis from a single image. In *IEEE Int. Conf. on Computer Vision and Pattern Recognition*, pages 184–189, Santa Barbara, 1998.
20. E. Mémin and P. Pérez. Dense estimation and object-based segmentation of the optical flow with robust techniques. *IEEE Trans. Image Processing*, 7(5):703–719, 1998.
21. E. Mémin and P. Pérez. Fluid motion recovery by coupling dense and parametric motion fields. In *Proc. Int. Conf. Computer Vision*, volume 3, pages 732–736, Corfou, Greece, 1999.
22. H. Nogawa, Y. Nakajima, and Y. Sato. Acquisition of symbolic description from flow fields: a new approach based on a fluid model. *IEEE Trans. Pattern Anal. Machine Intell.*, 19(1):58–63, 1997.
23. A. Ottenbacher, M. Tomasini, K. Holmlund, and J. Schmetz. Low-level cloud motion winds from Meteosat high-resolution visible imagery. *Weather and Forecasting*, 12(1):175–184, 1997.
24. C. Papin, P. Bouthemy, E. Mémin, and G. Rochard. Tracking and characterization of highly deformable cloud structures. In *Proc. Europ. Conf. Computer Vision*, volume 2, pages 428–442, Dublin, June 2000.
25. A.R. Rao and R.C. Jain. Computerized flow analysis: oriented texture fields. *IEEE Trans. Pattern Anal. Machine Intell.*, 14(7):693–709, 1992.

26. J. Schmetz, K. Holmlund, J. Hoffman, B. Mason, V. Gaertner, A. Koch, and L.V. De Berg. Operational cloud-motion winds from Meteosat infrared images. *Journal of Applied Meteorology*, 32:1206–1225, 1993.
27. J. Shukla and R. Saha. Computation of non-divergent streamfunction and irrotational velocity potential from the observed winds. *Monthly weather review*, 102:419–425, 1974.
28. J. Simpson and J. Gobat. Robust velocity estimates, stream functions, and simulated Lagrangian drifters from sequential spacecraft data. *IEEE trans. on Geosciences and Remote sensing*, 32(3):479–492, 1994.
29. S.M. Song and R.M. Leahy. Computation of 3D velocity fields from 3D cine and CT images of human heart. *IEEE trans. on medical imaging*, 10(3):295–306, 1991.
30. Q. Yang, B. Parvin, and A. Mariano. Feature based visualization of geophysical data. *Geophysical Research Letters*, 2:331–334, January 2001.
31. L. Zhou, C. Kambhamettu, and D. Goldgof. Fluid structure and motion analysis from multi-spectrum 2D cloud images sequences. In *Proc. Conf. Comp. Vision Pattern Rec.*, volume 2, pages 744–751, Hilton Head Island, South Carolina, USA, 2000.

Appendix

Considering a domain $\mathcal{D}$ delineated by a circle $\partial\mathcal{D}$ of radius R and the domain $\overline{\mathcal{D}}$ exterior to the disk, we show in this appendix that the derivative with respect to R of

$$\iint_{\mathcal{D}} f(x,y,R)dxdy + \iint_{\overline{\mathcal{D}}} g(x,y,R)dxdy, \tag{48}$$

where f and g coincide on circle $\partial\mathcal{D}$, is

$$\frac{\partial}{\partial R}\left(\iint_{\mathcal{D}} f(x,y,R)dxdy + \iint_{\overline{\mathcal{D}}} g(x,y,R)dxdy\right) = \iint_{\mathcal{D}} \frac{\partial f(x,y)}{\partial R}dxdy + \iint_{\overline{\mathcal{D}}} \frac{\partial g(x,y)}{\partial R}dxdy = 0. \tag{49}$$

Let us first consider the function:

$$H(R) = \iint_{\mathcal{D}} f(x,y,R)dxdy.$$

We want to compute the partial derivative $\frac{\partial H}{\partial R}$. In polar coordinate with origin the center of disk $\mathcal{D}$, this derivative is defined by (with slight abuse of notation $f(r,\theta,R)$

stands for $f(r\cos\theta, r\sin\theta, R)$):

$$\begin{aligned}
H'(R) &= \lim_{h\to 0}\frac{1}{h}\left[\int_0^{2\pi}\int_0^{R+h} f(r,\theta,R+h)rdrd\theta - \int_0^{2\pi}\int_0^{R} f(r,\theta,R)rdrd\theta\right]\\
&= \lim_{h\to 0}\frac{1}{h}\left[\int_0^{2\pi}\int_0^{R+h} f(r,\theta,R+h)rdrd\theta - \int_0^{2\pi}\int_0^{R} f(r,\theta,R+h)rdrd\theta\right.\\
&\left.+\int_0^{2\pi}\int_0^{R} f(r,\theta,R+h)rdrd\theta - \int_0^{2\pi}\int_0^{R} f(r,\theta,R)rdrd\theta\right]\\
&= \lim_{h\to 0}\frac{1}{h}\left[\int_0^{2\pi}\int_R^{R+h} f(r,\theta,R+h)rdrd\theta + \int_0^{2\pi}\int_0^{R} f(r,\theta,R+h) - f(r,\theta,R)rdrd\theta\right]\\
&= \int_0^{2\pi} f(R,\theta,R)Rd\theta + \int_0^{2\pi}\int_0^{R}\frac{\partial f(r,\theta,R)}{\partial R}rdrd\theta = \int\limits_{\partial\mathcal{D}} f + \iint\limits_{\mathcal{D}}\frac{\partial f}{\partial R}.
\end{aligned} \tag{50}$$

The derivation of function

$$J(R) = \iint\limits_{\overline{\mathcal{D}}} g(x,y,R)dxdy,$$

is then readily obtained by noting that

$$J(R) = \iint\limits_{\Omega} g - \iint\limits_{\mathcal{D}} g.$$

The derivation of the first term in the right hand side yields $\iint\limits_{\Omega}\frac{\partial g}{\partial R}$ and the one of the second term is similar to the one of $H(R)$:

$$\begin{aligned}
J'(R) &= \iint\limits_{\Omega}\frac{\partial g}{\partial R} - \left[\int\limits_{\partial\mathcal{D}} g + \iint\limits_{\mathcal{D}}\frac{\partial g}{\partial R}\right]\\
&= \iint\limits_{\overline{\mathcal{D}}}\frac{\partial g}{R} - \int\limits_{\partial\mathcal{D}} g.
\end{aligned} \tag{51}$$

By continuity at circular boundary $\partial\mathcal{D}$, implying $\int\limits_{\partial\mathcal{D}} f = \int\limits_{\partial\mathcal{D}} g$ we get:

$$\frac{\partial}{\partial R}\left(\iint\limits_{\mathcal{D}} f + \iint\limits_{\overline{\mathcal{D}}} g\right) = \iint\limits_{\mathcal{D}}\frac{\partial f(R)}{\partial R} + \iint\limits_{\overline{\mathcal{D}}}\frac{\partial g(R)}{\partial R}. \quad \blacksquare \tag{52}$$